Solid State Ionics 411 (2024) 116578

Contents lists available at ScienceDirect

Solid State Ionics

journal homepage: www.elsevier.com/locate/ssi

Suitability of NaI complexed sodium alginate-polyvinyl alcohol biodegradable polymer blend electrolytes for electrochemical device applications: Insights into dielectric relaxations and scaling studies

Vipin Cyriac [a], Ismayil [a,*], Kuldeep Mishra [b], Y.N. Sudhakar [c], Z.E. Rojudi [d], Saraswati P. Masti [e], I.M. Noor [d,f]

[a] Department of Physics, Manipal Institute of Technology, Manipal Academy of Higher Education, Manipal 576104, Karnataka, India
[b] Symbiosis Institute of Technology (SIT), Symbiosis International (Deemed University) (SIU), Pune 412115, Maharashtra, India
[c] Department of Chemistry, Manipal Institute of Technology, Manipal Academy of Higher Education, Manipal 576104, Karnataka, India
[d] Ionic Materials and Energy Devices Laboratory, Physics Department, Faculty of Science, Universiti Putra Malaysia, 43400 UPM Serdang, Selangor Darul Ehsan, Malaysia
[e] Department of Chemistry, Karnataka University's Karnataka Science College, Dharwad, Karnataka 580001, India
[f] Physics Division, Centre for Foundation Studies in Science of Universiti Putra Malaysia, Universiti Putra Malaysia, 43400 Serdang, Selangor Darul Ehsan, Malaysia

ARTICLE INFO

Keywords:
Polymer electrolytes
Ionic conductivity
Scaling studies
Dielectric spectroscopy

ABSTRACT

This study focuses on an in-depth analysis of the relaxation phenomenon of sodium iodide (NaI)-complexed solid polymer electrolyte membranes based on sodium alginate (NaAlg) and poly (vinyl alcohol) (PVA) using various formalisms to test the suitability of these membranes for electrochemical device applications. The incorporation of NaI led to an increase in the ionic conductivity from $(6.12 \pm 0.14) \times 10^{-8}$ Scm^{-1} (PNI0, pure blend) to $(4.27 \pm 0.09) \times 10^{-6}$ (PNI10, 10 wt% of NaI). Deep insights into ion transport parameters at ambient and high temperatures, obtained from Nyquist plot fitting revealed the dependency of dc conductivity on carrier concentration (n) rather than mobility (μ) and diffusion coefficient (D). Scaling studies based on AC conductivity and tangent loss revealed the collapse of conductivity and tangent loss plots into a single master curve, implying that the optimum sample obeys time-temperature superposition principle (TTSP). The temperature dependence of the Jonscher's exponent indicates that the conduction mechanism can be effectively represented by the Quantum Mechanical Tunneling model (QMT). The non-Debye behavior exhibited by the samples can be elucidated through the electric modulus formalism and confirmed dielectric properties of the electrolytes, as demonstrated by the incomplete semicircular arcs observed in the Argand plots. Moreover, the prepared samples were completely biodegradable, indicating the eco-friendly nature of the electrolytes.

1. Introduction

Classical electrolytes consist of ionizable components, such as KOH and $LiPF_6$, dissolved in solvents with high dielectric constants, such as water and ethylene carbonate. In 1973, Fenton et al. [1] made a significant discovery involving the dissolution of alkali salts in poly (ethylene oxide) (PEO), leading to the emergence of the field of solid polymer electrolytes. In recent decades, the research community has devoted significant attention to the development of novel polymer electrolytes (PEs) owing to their vast potential for various applications, including electrochemical/electrical power generation, storage, and conversion systems. These systems encompass a broad range of technologies such as supercapacitors [2], fuel cells [3], dye-sensitized solar cells [4], rechargeable batteries [5] and electrochemical sensors [6].

Extensive studies have been conducted on employing polymer electrolytes instead of traditional separators in rechargeable batteries. The shift towards polymer electrolytes is largely driven by their ability to enhance safety measures, effectively mitigating the risks associated with electrolyte leakage, internal shorting, the use of corrosive solvents, emission of toxic gases, and the formation of inflammable compounds on the electrode interfaces [7].

Although PEs offer various advantages, they exhibit low ionic conductivity at room temperature [8]. Polymer electrolytes often

* Corresponding author.
E-mail address: ismayil.mit@manipal.edu (Ismayil).

https://doi.org/10.1016/j.ssi.2024.116578
Received 8 March 2024; Received in revised form 18 April 2024; Accepted 29 April 2024
Available online 4 May 2024

demonstrate limited mechanical strength, leading to brittleness and susceptibility to cracking and tearing [9]. Additionally, some polymer electrolytes can react with the electrodes in batteries, causing corrosion and other issues. To meet the demands of commercial applications, solid polymer electrolytes (SPEs) must exhibit high ionic conductivity ($>10^{-4}$ S cm^{-1}), favorable mechanical properties, and exceptional stability at electrode interfaces. These aspects are fundamental requirements for PEs [10].

Extensive research has been conducted on various natural and synthetic polymers for the development of solid polymer electrolytes. Natural polymers, including starch, chitosan, sodium alginate, and carboxymethyl cellulose (CMC), have received significant attention owing to their abundance and suitability for the preparation of polymer-based electrolytes. Furthermore, synthetic polymers such as polyvinyl alcohol (PVA), polyethylene oxide (PEO), and polyvinylidene fluoride (PVdF) have demonstrated significant ionic conductivity properties, making them suitable for incorporation into SPE systems. To further improve ionic conductivity and various physicochemical characteristics, researchers have adopted diverse techniques, including polymer blending, grafting of copolymers, and integration of ceramic substances and plasticizers [11]. Among these methods, polymer blending is extensively used because of its ease of preparation. Furthermore, the properties can be tailored by changing the composition of the individual components of the polymer blends.

In this study, sodium alginate (NaAlg) was selected as the primary component of the polymer blend because of its rigid molecular chain and excellent ability to form films. It has been extensively utilized and thoroughly investigated for its potential applications as a drug carrier in the field of biomedicine [12]. Sodium alginate can serve as a host for polymer electrolytes because it contains numerous electronegative atoms, specifically oxygen atoms in the −COO and − OH groups, which can act as complexing sites for dissolved salts. Although NaAlg is rigid and brittle, it can be blended with poly (vinyl alcohol) (PVA), a highly elastic and biocompatible material. This blend can improve the mechanical properties of NaAlg, making it a suitable candidate for various applications [13]. Therefore, PVA was chosen as the secondary component in this study because it contains–OH groups that can form hydrogen bonds with the functional groups of NaAlg, resulting in good compatibility [14]. Furthermore, several studies have explored the electrochemical device applications of NaAlg, PVA, and their blended polymer electrolyte membranes, focusing on their compatibility with lithium [14], sodium [15], potassium [16], and proton-based [17–19] systems.

Many studies have demonstrated the key advantages of NaI in improving the overall performance of polymer electrolytes employed in dye-sensitized solar cells. For instance, they have been found to improve the energy-conversion efficiency of solar cells [20]. NaI in polymer electrolytes improves the solar cell performance owing to easier penetration through the TiO_2 nanoporous layer and better adhesion with the electrodes [21]. Sodium iodide in polymer electrolytes leads to increased conductivity, decreased relaxation time, and faster ion dynamics [22]. NaI is relatively stable at room temperature and can withstand moderate heating without decomposing. This stability can be advantageous in situations where the electrolyte must operate under varying conditions. In addition, sodium iodide is highly soluble in water, which makes it suitable for the preparation of aqueous solutions and electrolytes. Hence, continuing from our previous study [23], this work systematically investigated the impact of the NaI dopant on the microstructural properties of the NaAlg-PVA blend and the ionic dynamics through various formalisms such as Nyquist plot, AC conductivity, dielectric, and modulus formalism. The scaling approach (time-temperature superposition principle) was employed to determine whether the ion conduction mechanism adheres to a common mechanism at elevated temperatures.

2. Experimental methods

2.1. Materials

The following chemicals were used without further purification to prepare the solid polymer electrolyte membranes: Sodium Alginate (NaAlg, viscosity>1000 cPs for 1% aq. Soln. at 20 °C), poly (vinyl alcohol) (PVA, M_w = 85,000 g mol^{-1}, 86% hydrolyzed), and sodium iodide (NaI, M_w=149.89 g mol^{-1}). All the polymer powders were purchased from S.D. Fine Chem Limited, Mumbai, and NaI was procured from Merck Life Science Limited, Mumbai, India.

2.2. Preparation of solid polymer electrolyte membranes

Solid polymer electrolytes were prepared using a cost-effective conventional solution casting technique. In this study, a polymer blend (with a weight ratio of NaAlg/PVA of 60:40) and NaI salt were added at various concentrations, as listed in Table 1. The composition of the 60 wt% NaAlg: 40 wt% PVA was chosen based on the optimized ratio reported by Sheela et al. [14]. Owing to difficulties in forming stable freestanding films, the doping levels were capped at 20 wt%. All the materials were accurately weighed and combined in a beaker containing 100 ml of double-distilled water. The mixture was allowed to swell for 6 h to facilitate the stirring process and then stirred using a magnetic bar at 40 °C overnight. The uniform mixture was subsequently spread onto polyethylene petri dishes and placed inside a hot-air oven maintained at a temperature of 40 °C. The drying process took approximately 3 days. The sample was then peeled off and stored in a vacuum desiccator with a silica desiccant until further characterization. The flowchart of the preparation method is shown in Fig. 1.

2.3. Sample characterisations

2.3.1. Fourier-transform infrared (FTIR) spectroscopy

The interaction between the NaI salt and NaAlg/PVA blend was analyzed by observing alterations in the infrared spectra using a SHIMADZU IRPrestige-21 ATR-FTIR instrument. The resolution was set to 4 cm^{-1}, and the spectra were recorded at room temperature in transmittance mode.

2.3.2. X-ray diffraction (XRD)

The structural changes resulting from the incorporation of salt into the blend polymer matrix were investigated using XRD (Rigaku Miniflex 600, 5th Gen). Cu kα radiation with a wavelength λ = 1.54 Å was irradiated onto the sample in the range of $5^\circ < 2\theta < 90^\circ$, at a scanning rate of 2° min^{-1}.

2.3.3. Electrochemical impedance spectroscopy (EIS)

To understand the impact of dopant concentration on ionic conductivity, EIS was conducted. The measurements were performed using a HIOKI IM3570 Impedance Analyzer. The specimens were positioned between stainless steel electrodes designed to block ion passage. An alternating current (AC) voltage of 10 mV with a frequency range of 100 Hz– 4.5 MHz was applied across the sample. These measurements were conducted over a temperature range from room temperature (25 °C) to 120 °C. From these measurements, real (Z') and negative imaginary

Table 1
Sample designations with compositions of NaAlg, PVA, and NaI.

Designation	NaAlg (g)	PVA (g)	NaI (g)	NaI (wt%)
PNI0	1.20	0.80	0	0
PNI5	1.14	0.76	0.10	5
PNI10	1.08	0.72	0.20	10
PNI15	1.02	0.68	0.30	15
PNI20	0.96	0.64	0.40	20

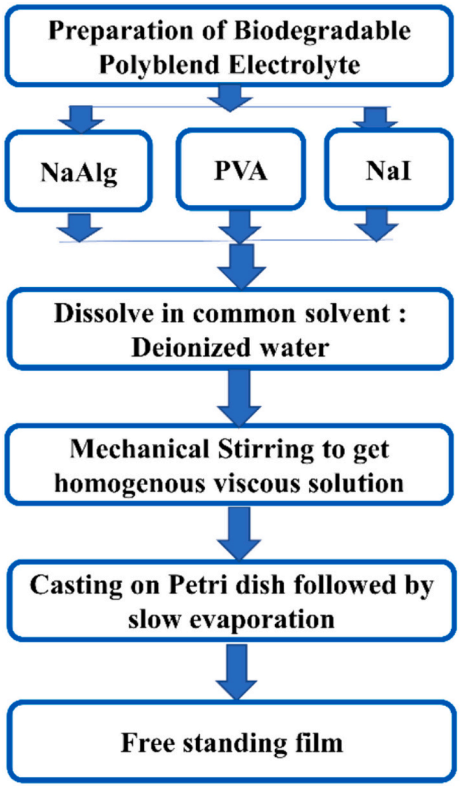

Fig. 1. Sample preparation flowchart.

($-Z''$) impedances were obtained. Eqs. (1) and (2) were used to convert the impedance data into a dielectric format to understand the ion dynamics occurring in SPEs.

The real (ε') and imaginary (ε'') parts of the complex permittivity were deduced using eqs. (1) and (2).

$$\varepsilon' = \frac{Z''}{\omega C_o\left(Z'^2 + Z''^2\right)} \tag{1}$$

$$\varepsilon'' = \frac{Z'}{\omega C_o\left(Z'^2 + Z''^2\right)} \tag{2}$$

In Eqs. (1) and (2), C_o is the vacuum capacitance. The real (M') and imaginary (M'') parts of the complex modulus were constructed using eqs. (3) and (4).

$$M' = \frac{\varepsilon'}{\varepsilon'^2 + \varepsilon''^2} \tag{3}$$

$$M'' = \frac{\varepsilon''}{\varepsilon'^2 + \varepsilon''^2} \tag{4}$$

Tangent loss (tan δ) of SPEs was determined using eq. (5).

$$tan\delta = \frac{\varepsilon''}{\varepsilon'} \tag{5}$$

2.3.4. Thermal studies

Differential scanning calorimetry (DSC) and thermogravimetric analysis (TGA) were employed to observe the thermal characteristics and thermal stability of the NaAlg/PVA–NaI system. Differential scanning calorimetry (DSC) measurements were conducted using a SHIMADZU DSC-60 PLUS instrument. Specimens with a masses in the range of 5–8 mg were positioned in sealed platinum crucibles and subjected to a consistent heating process from ambient temperature to 250 °C, with a temperature increase of 10 °C per minute. Thermogravimetric analysis (TGA) was performed using a Hitachi STA7200 TGA-DTA instrument. A sample weighing 5 mg was placed in the sample pan and heated from room temperature to 500 °C under N_2 gas atmosphere at a flow rate of 20 ml min^{-1}.

2.3.5. Scanning electron microscopy (SEM)

The morphological changes of the SPE surface were studied using a Zeiss EVO 18 SEM. The specimen was covered with a fine gold layer using a Quorum Gold sputtering device for 5 min to reduce the impact of charging on the sample. Moreover, elemental mapping was conducted to assess the distribution of different elements within the polymer matrix.

2.3.6. Atomic force microscopy (AFM)

Atomic force microscopy was carried out to evaluate the surface morphology of the polymer films using the root mean square roughness. Innova SPM Atomic Force Microscope was used. Tapping mode was employed in a scanning area of 5 μm × 5 μm.

2.3.7. Linear sweep voltammetry (LSV)

LSV was conducted to determine the electrochemical stability window (ESW) of the electrolyte, utilizing a CH600E galvanostat. The electrolyte film was placed between sodium amalgam (NaHg) and stainless steel (SS) electrodes, forming a cell configuration of NaHg|SPE|SS. The voltage was progressively increased from 0 to 5.5 *V* across the sample at a scanning speed of 5 mV s^{-1}, and the current passing through the sample was measured.

2.3.8. Transference number measurement (TNM)

Ion and electron transference numbers were determined through Wagner's polarization method [24] by applying a direct current (DC) voltage of 100 mV to a symmetric cell. The cell configuration was SS|SPE|SS. The current was measured over time using a Keithley 2636B source meter. The presence of SS blocking electrodes leads to a rapid decline in the initial current amplitude (I_i), indicative of ion polarization. Under steady-state conditions, the diffusion process balances the movement of ions which results in a stabilized current (I_f). The total ionic transference number was calculated using eq. (6).

$$t_{ion} = \frac{I_i - I_f}{I_i} \tag{6}$$

The electron transference number is given by eq. (7)

$$t_{elec} = 1 - t_{ion} \tag{7}$$

Eqs. (8) and (9) were used to calculate the ionic and electronic conductivities by utilizing the ion-electron transference number and electrolyte bulk conductivity (σ) obtained from the EIS measurements.

$$\sigma_{ionic} = t_{ion} \times \sigma \tag{8}$$

$$\sigma_{electronic} = t_{elec} \times \sigma \tag{9}$$

2.3.9. Mechanical properties

According to the ASTM standard D882, the tensile test method was employed to evaluate the mechanical properties of the SPE using a universal testing machine (Dak System Inc. 7200 series). A rectangular sample (5.0 cm × 2.5 cm) was placed between the tensile grips and pulled at a crosshead speed of 0.1 mm per minute. To assess the relationship between the variations in the mechanical characteristics and salt concentration, three identical samples were used in the experiment.

2.3.10. Biodegradability test

A soil burial test was conducted to assess the degradability of the highest conducting sample, following a previous report, with slight modifications [25]. The microflora was not altered to maintain a natural biodegradation environment. The sample of diameter 8 cm was dried and weighed (W_i). The sample was subsequently buried in garden soil to

a depth of 10 cm, with 10 ml of water dispensed daily [26]. The sample was periodically retrieved from the soil, cleaned, dried in oven and the final weight (W_f) was recorded. Cellulose and other nutrients present in the samples served as carbon and nitrogen sources for microbes. The addition of water facilitates the activation of soil microorganisms. The percentage of biodegradability (W_d) was calculated using eq. (10).

$$W_d = \frac{W_i - W_f}{W_i} \times 100\% \quad (10)$$

3. Results and discussions

3.1. FTIR spectroscopic studies

FTIR spectroscopy was employed to determine the interactions between different polymer components in the blend, as well as the interactions between the salts and the polymer blend. This was accomplished by examining alterations in both the wavenumber and intensity of the major vibrational bands observed in the spectra. Wavenumber changes falling within the resolution limit (4 cm^{-1}) of the FTIR instrument are not considered. The probable interaction between NaAlg and PVA is elaborated upon in references [14, 15]. These findings indicate the presence of intermolecular hydrogen bonding between the −OH groups of PVA and the −OH/COO^- groups of the NaAlg polymer. The FTIR spectra in transmittance mode of the PVA-NaAlg blends with various NaI concentrations are shown in Fig. 2.

Fig. 2 highlights eight distinct bands pertinent to the NaAlg/PVA blend system. The main vibrational bands of the NaAlg/PVA–NaI solid polymer electrolytes (SPEs) and their corresponding assignments are listed in Table 2. For the PNI0 sample, the OH stretching vibration is noted at 3275 cm^{-1}, CH_2 asymmetric vibration at 2941 cm^{-1}, C═O stretching vibration at 1710 cm^{-1}, asymmetric COO^- stretching vibration at 1594 cm^{-1}, symmetric −COO stretching vibration at 1410 cm^{-1}, −CH wagging at 1262 cm^{-1}, −COC− stretching associated with the glycosidic linkage at 1027 cm^{-1} and C − C stretching at 814 cm^{-1} [13,14,27–30]. The changes in the vibrational bands are seen as a function of the increase in NaI salt concentration. The main regions of interest were the oxygen atoms of the −OH and − COO groups in the NaAlg/PVA polymer matrix. The presence of functional groups containing oxygen atoms in the NaAlg/PVA blend polymer enabled the formation of a polymer-salt electrolyte. This was facilitated by the oxygen atoms acting as electron donors, thereby forming dative bonds with Na^+ ions from the doping salts [31].

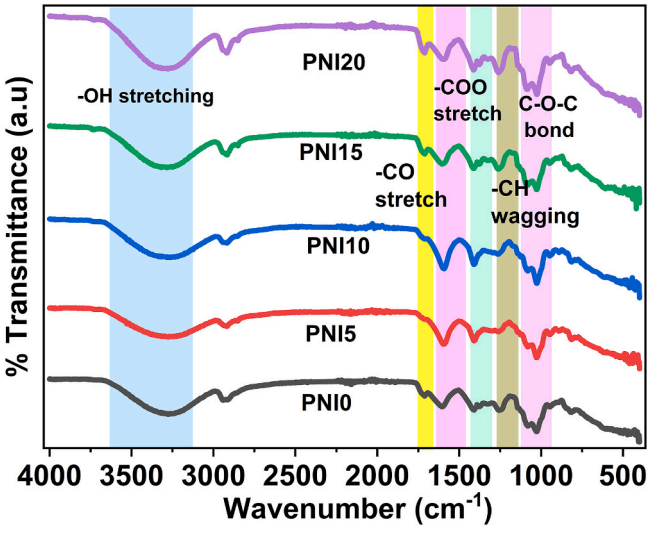

Fig. 2. FTIR spectra of NaAlg/PVA–NaI SPE in transmittance mode between 4000 cm^{-1} and 400 cm^{-1}.

Table 2
FTIR functional groups of NaAlg/PVA-NaI SPEs with corresponding wavenumbers.

Functional group	Wavenumber (cm^{-1})				
	PNI0	PNI5	PNI10	PNI15	PNI20
O − H stretching	3275	3291	3310	3344	3349
C − H_2 asymmetric stretching	2941	2941	2942	2942	2943
C=O Stretching	1711	1712	1714	1711	1711
Asymmetric COO− stretching	1605	1601	1606	1605	1606
Symmetric COO− stretching	1410	1409	1410	1413	1412
O − H bending	-	1376	1376	1379	1376
C − H wagging	1257	1261	1261	1267	1267
COC stretching of glycosidic bond	1027	1028	1027	1027	1026
C − C stretching	814	814	814	815	816

In polymer electrolyte systems, sodium iodide dissociates into Na cations and I anions, which subsequently coordinate with atoms in the host structure of the polymer. Na^+ is expected to interact with the oxygen atom of the C═O group in NaAlg due to the electronegative nature of the oxygen atom. However, there was no shift in the band wavenumber (beyond the resolution of the instrument) corresponding to C═O or − COO stretching (Table 2). Therefore, the coordination of Na^+ from the doping salt was not considered to occur at these two functional groups of NaAlg. Although the C═O group does not directly coordinate with the free ions from the dissociated salt, it participates in intermolecular hydrogen bonds between the −OH group of PVA and the COO group of the NaAlg polymer [14,32]. As indicated in Fig. 2, the wavenumber of the −OH group shifted from 3275 cm^{-1} to 3349 cm^{-1}, which suggests the formation of a coordinate bond between the sodium ions and the oxygen atoms in the −OH group. Since the shift is >4 cm^{-1}, this band is considered a prominent interaction of sodium ions with the polymer matrix.

The wavenumber corresponding to −OH bending (~1376 cm^{-1}) appeared in the salt-doped samples but was absent in the NaAlg/PVA blend. The absence of these bands in the pure blend polymer implies their involvement in the formation of intermolecular or intramolecular hydrogen bonds among the monomer units. Conversely, the emergence of these bands in the salt-doped system suggests that the dopant participates in the formation of hydrogen bonds with polymer units [33]. Moreover, the increase in the wavenumber of −CH wagging from 1257 cm^{-1} to 1267 cm^{-1} indicates the interaction of the I^- anion with the $-CH_2$ group of the polymer blend through a hydrogen bond [34]. Hydrogen bond formation arises from the interaction between an electron-deficient hydrogen atom and an atom with high electron density, typically a highly electronegative atom such as O or Cl. Intermolecular hydrogen bond interactions between molecules can be represented as X-H—Y, where X and Y are highly electronegative atoms that contain electron pairs. However, hydrogen bond interactions can be extended to several other systems via X-H—Y interactions, where X is not highly electronegative. It is sufficient that the X − H bond to be slightly polar. This requirement includes groups such as C − H and P − H as well as various metal halide groups [35]. Thus, the interaction of I^- with the −CH group is justified. The changes in the intensities of the bands, as indicated in Fig. 2, also suggest complexation of the salt with the polymer matrix. All the possible interactions are shown in Fig. 3.

3.2. X-ray diffraction (XRD)

X-ray diffraction (XRD) was used to assess the structural modifications resulting from the integration of the NaI salt into the polymer matrix. XRD patterns of the NaI and NaAlg/PVA-NaI solid polymer electrolytes (SPEs) are presented in Figure 4. The NaI salt showed multiple sharp peaks at 2θ angles of 23.67°, 29.74°, 32.69°, and 37.84°, highlighting its crystalline structure. In the XRD profiles of the SPE samples ranging from PNI0 to PNI20, no significant peaks attributable to the salt were detected, implying the complete dissolution of the salt

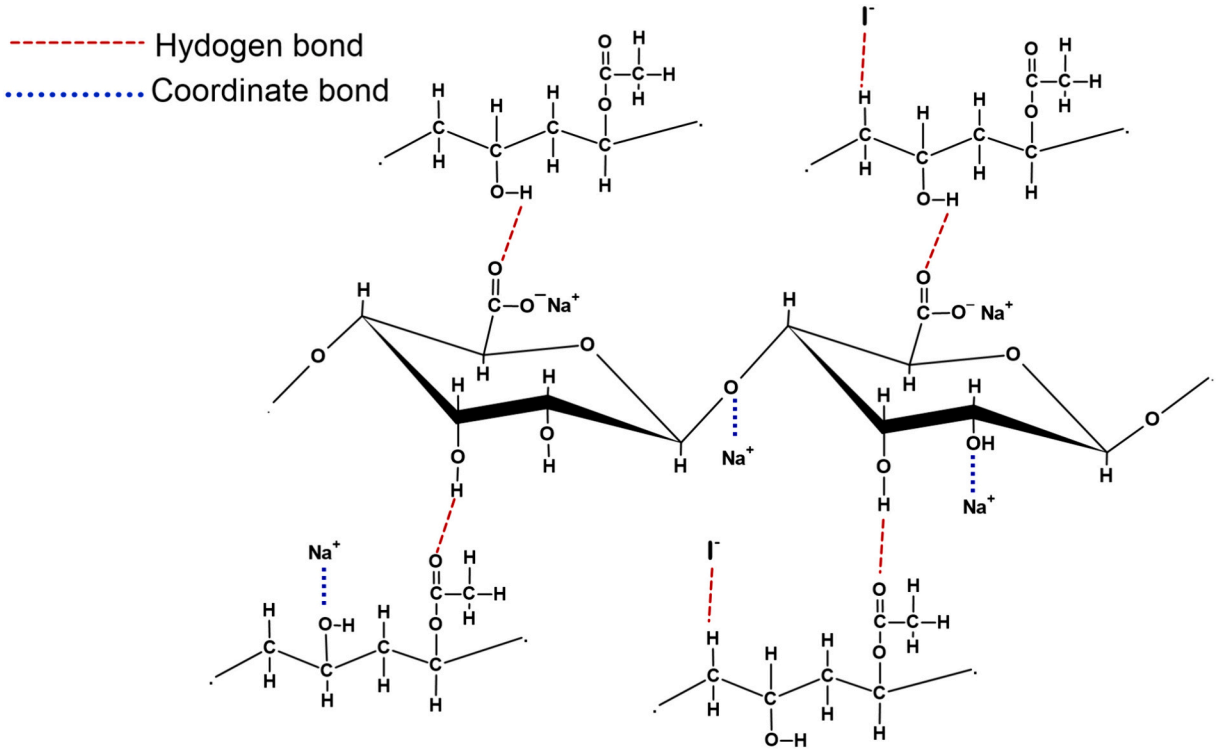

Fig. 3. Possible interactions between the NaI dopant and NaAlg/PVA polymer blend matrix.

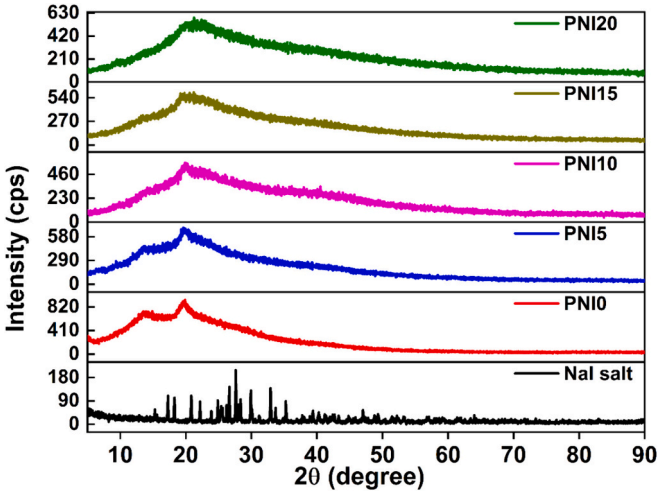

Fig. 4. XRD pattern for NaAlg/PVA-NaI SPEs.

within the polymer framework [36]. The PNI0 film (salt-free electrolyte) displayed a semi-crystalline nature, with two dominant crystalline peaks centered at 2θ values of 13.80°and 20.00° [37]. According to the criteria set forth by Hodge et al., the reduction in the intensity of the peaks located at 2θ = 13.80°and 20.00°, which are characteristic of PVA, coupled with an increase in peak width, signifies a shift towards a more amorphous structure within the polymer matrix due to the incorporation of the salt [38]. The observed decrease in peak height and the concurrent broadening of the peak width in the X-ray diffraction patterns suggest that the NaI salt disrupts the intermolecular and intramolecular hydrogen bonds within the polymer matrix. This disruption facilitates the formation of a complex between the polymer blend and the salt, altering the structural dynamics of the system. This observation aligns with the FTIR findings, where the absence of the −OH bending band was observed in the polymer blend and its reappearance in the salt-doped samples.

To confirm the pronounced amorphous nature of the films complexed with salt, XRD deconvolution was performed over the entire XRD spectrum to distinguish the crystalline and amorphous peaks within the broad halo. The deconvolution procedure was detailed in our previous report [39]. Given that the blend was composed of NaAlg and PVA components, the XRD spectrum of the blend exhibited a convolution of peaks originating from both NaAlg and PVA. This overlay of peaks reflects the combined structural characteristics of the two components within the blend. The same event is illustrated in Fig. 5 [23]. The degree of crystallinity was calculated using Eq. (11).

$$\chi = \frac{\text{Area under all crystalline peaks}}{\text{Area under all peaks}} \times 100\% \tag{11}$$

The crystallinity obtained from XRD deconvolution of the NaAlg-PVA-NaI SPE system is shown in Fig. 5. The crystallinity decreased with increasing salt doping and reached a minimum of 3.89% for the PNI10 sample, contributing to easier ion migration and leading to a high ionic conductivity. This increase in the amorphous nature was attributed to the disruption of the crystalline phase of the polymer matrix by the salt. This disruption occurs because of the formation of new bonds between the salt and polymer functional groups, leading to the breakage of existing intermolecular and intramolecular hydrogen bonds, as discussed in the FTIR study [40].

For the samples with >10 wt% of salt concentration, the crystallinity of the polymer matrix increases. However, peaks corresponding to the salt characteristics were not observed in the XRD patterns of PNI15 and PNI20. This implies that the salt was completely dissociated into Na^+ and I^- ions, and these ions might have reassociated, forming contact pairs. This reassociation could block ion migration, leading to a decrease in conductivity and an increase in crystallinity.

3.3. Impedance spectra at room and elevated temperatures

Complex impedance spectroscopy is a potent technique for investigating the electrical properties of polymer electrolytes over the use of

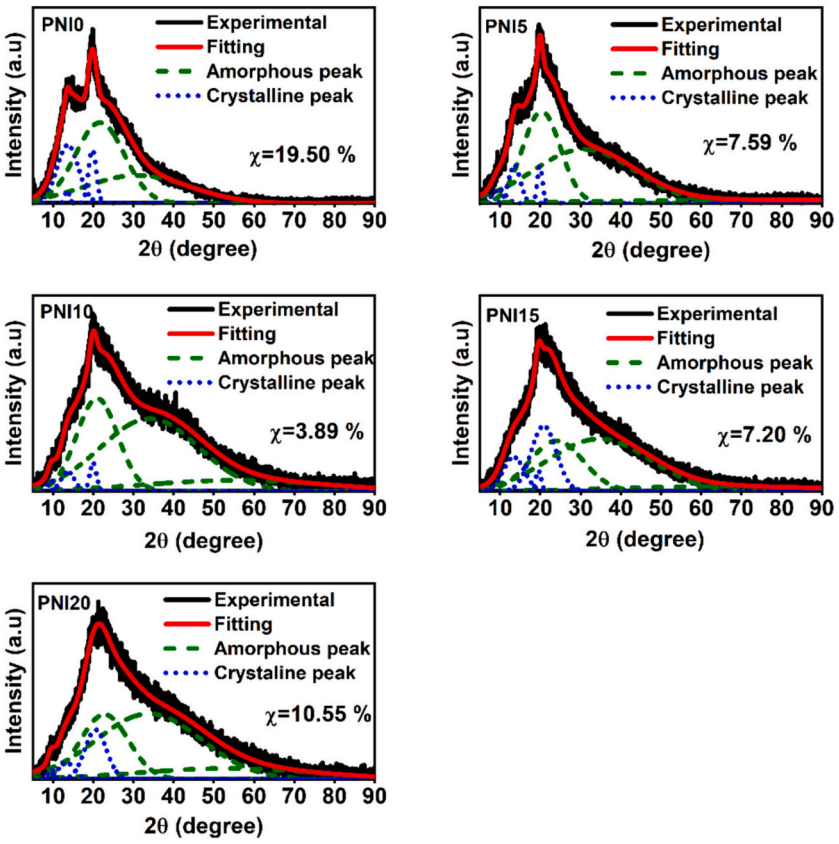

Fig. 5. Deconvoluted XRD spectra of NaAlg/PVA-NaI SPEs.

straightforward direct current (DC) approach. This effectiveness stems primarily from charge polarization occurring at the electrode-electrolyte interface, sample phase boundaries, or a combination of both. The polarization effect can be mitigated by applying a small alternating current (AC) voltage across the sample and subsequently measuring the impedance as a function of frequency. The real (Z') and negative imaginary ($-Z''$) parts of the impedance are represented by Nyquist plots in Fig. 6. The Nyquist plot consisted of a depressed semicircle at high frequencies and a tilted spike at low frequencies. The non-Debye nature of the material is demonstrated by the semicircle's center below the real axis [41]. The depressed semicircle is related to the bulk conduction and capacitance of the electrolyte. The presence of a tilted spike in the plot is attributed to electrode polarization, which is characteristic of the diffusion process [42]. The spike was inclined at an angle of $<90^{\circ}$ with respect to the Z' axis, indicating the roughness of the electrode-electrolyte interface [43]. Because ion-blocking electrodes are used for

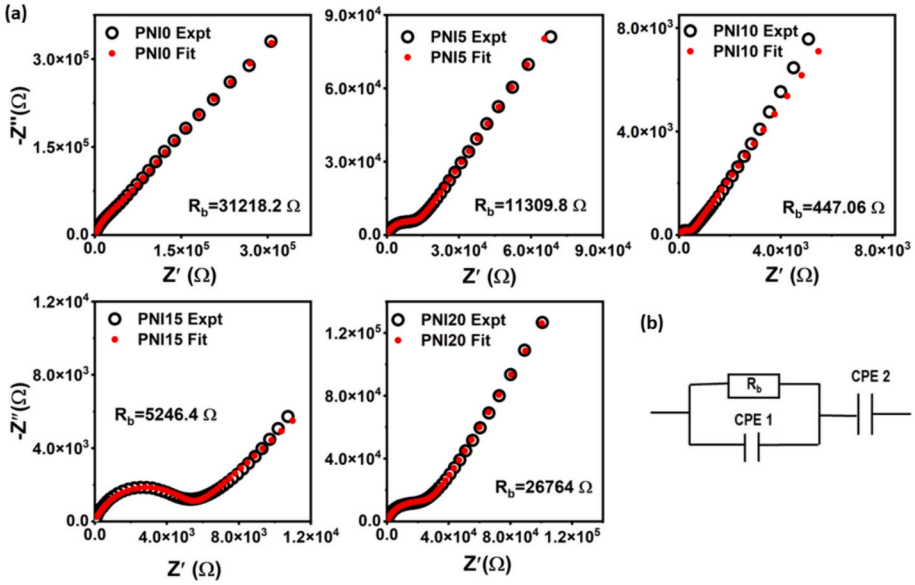

Fig. 6. (a) Experimental (black circles) Nyquist plot (at 25 °C) for NaAlg/PVA-NaI SPEs with corresponding fitted data (red dots) and (b) electrical equivalent circuit used to fit the Nyquist plot. (For interpretation of the references to colour in this figure legend, the reader is referred to the web version of this article.)

measurements, the electrode-electrolyte interface can be regarded as an electrical double-layer capacitance.

The diameter of the semicircle decreases with increasing salt concentration and reaches a minimum for the PNI10 sample, indicating the lowest bulk resistance. With a further increase in salt concentration, the diameter of the semicircle increased, indicating an increase in the bulk resistance. The bulk resistance was determined at the intersection between the depressed semicircle and the tilted spike. The utilization of electrical equivalent circuit (EEC) representation is widespread because of its ability to provide a comprehensive depiction of the system across a broad range of applied frequencies. Thus, the Nyquist plot in Fig. 6(a) can be fitted by an EEC consisting of a constant phase element (CPE) in series with a parallel combination of the bulk resistance and another CPE (Fig. 6(b)). The constant phase element is used instead of the capacitance to represent the deviation of the spike from its ideal behavior (a vertical spike parallel to the imaginary axis). The impedance of the CPE is given by $Z_{CPE} = \frac{k}{(j\omega)^p}$, where k^{-1} is the capacitance of the CPE, and p is the fractional quantity ($0 < p < 1$) associated with the deviation of the spike from the $-Z''$ axis in the Nyquist plot [44]. The impedance of the equivalent circuit in Fig. 6(b) is given by eq. (12).

$$Z^* = Z' + j(-Z'') = \frac{R_b}{1 + R_b k_1^{-1}(j\omega)^{p_1}} + \frac{k_2}{(j\omega)^{p_2}} \tag{12}$$

Simplifying eq. (12) and equating the real and imaginary parts yields eqs. (13) and (14), respectively.

$$Z' = \frac{R_b + R_b^2 k_1^{-1}\omega^{p_1} cos\left(\frac{\pi p_1}{2}\right)}{1 + 2R_b k_1^{-1}\omega^{p_1} cos\left(\frac{\pi p_1}{2}\right) + R_b^2 k_1^{-2}\omega^{2p_1}} + \frac{cos\left(\frac{\pi p_2}{2}\right)}{k_2^{-1}\omega^{p_2}} \tag{13}$$

$$-Z' = \frac{R_b + R_b^2 k_1^{-1}\omega^{p_1} sin\left(\frac{\pi p_1}{2}\right)}{1 + 2R_b k_1^{-1}\omega^{p_1} cos\left(\frac{\pi p_1}{2}\right) + R_b^2 k_1^{-2}\omega^{2p_1}} + \frac{sin\left(\frac{\pi p_2}{2}\right)}{k_2^{-1}\omega^{p_2}} \tag{14}$$

Eqs. (13) and (14) were used to fit the Nyquist plots [44], and the bulk resistance values were determined and tabulated in Table 3. Using this value of R_b, the electrolyte conductivity is calculated using eq. (15) and tabulated in Table 3.

$$\sigma = \frac{t}{R_b A} \tag{15}$$

In eq. (15), t is the sample thickness and A is the effective area of contact.

The room temperature bulk conductivity is highest for PNI10 and is on the order of 10^{-6} S cm^{-1}. With a further increase in the salt concentration, the conductivity decreased owing to salt reassociation. Now, the ionic conductivity at high temperatures is discussed.

The ionic conductivity against temperature was studied to analyze the ion transport mechanism in NaAlg-PVA-NaI SPEs. Fig. 7 shows the Arrhenius plot for NaAlg-PVA-NaI SPEs obtained using Eq. (16).

$$\sigma(T) = Bexp\left(-\frac{E_a}{k_b T}\right) \tag{16}$$

In eq. (16), the constant B is directly related to the quantity of charge carriers and E_a signifies the activation energy required. The Boltzmann constant is denoted by k_b, and T stands for the absolute temperature measured in Kelvin. As the temperature increased, the number of free ions within the polymer increased, leading to enhanced ionic conductivity in the electrolyte. The E_a for all electrolyte was calculated using (16) and listed in Table 3. The relationship between the activation energy and ionic conductivity is inversely proportional. The PNI10 electrolyte with a higher ionic conductivity exhibits a lower activation energy, suggesting that less energy is required to initiate ion migration. A reduced E_a leads to a narrower band gap, making it easier for ions to move, thus enhancing ionic conductivity [8]. Furthermore, a lower E_a is essential for efficient ion migration, contrasting with the higher energy needed for the conduction process in the sample.

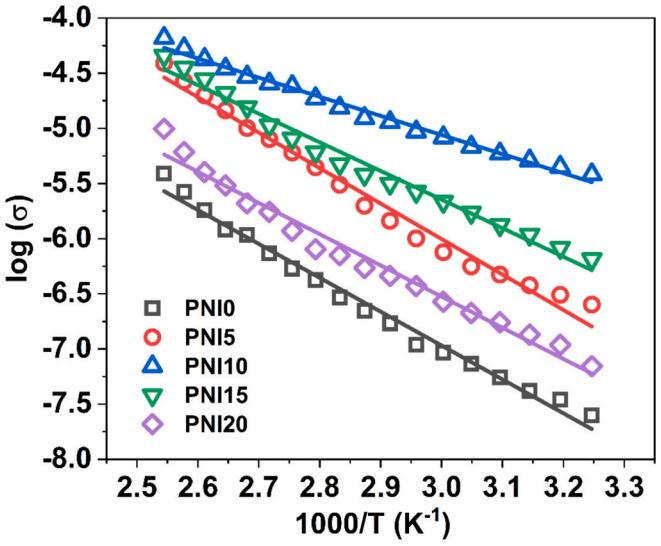

Fig. 7. Arrhenius plot of NaAlg/PVA-NaI SPEs.

3.4. AC conductivity studies

Fig. 8 depicts the variation in AC conductivity as a function of frequency. There are three distinct regions: (i) a low-frequency dispersion region (below 10 kHz), (ii) a mid-frequency plateau region (region between 10 kHz–100 kHz), and (iii) a high-frequency dispersion region (above 100 kHz). The dispersion in AC conductivity indicates an increase in AC conductivity with frequency. The plateau region suggests that the AC conductivity is independent of the sweeping frequency. The low conductivity in the low-frequency dispersion region is primarily attributed to the majority of ions being situated at the electrode-electrolyte interface, making fewer ions available in the bulk. The Jonscher Universal Power Law (UPL) was applied to investigate the conduction mechanism in the polymer electrolyte. This framework is pivotal for interpreting the frequency-dependent AC conductivity observed in solid polymer electrolytes (SPEs) and offers a deeper understanding of the electrical properties and behaviors of these materials. This law suggests that the total ac conductivity $\sigma(\omega)$ is equal to the sum of the DC conductivity σ_{dc} and the frequency dependent conductivity

Table 3
Values of bulk resistance obtained by EEC modelling (R_b), DC conductivity from EEC modelling (σ_{dc}), conductivity from AC spectra (σ_{ac}), C, s, conductivity relaxation time (τ), activation energy (E_a) and Regression coefficient (R^2) for PNI samples at 25 °C.

Sample	R_b (Ω)	σ_{dc} (S cm^{-1})	σ_{ac} (S cm^{-1})	C ($\times 10^{-12}$)	s	τ ($\times 10^{-4}$ s)	E_a (eV)	R^2
PNI0	31,218.20 ± 762.27	(6.12 ± 0.14) × 10^{-8}	(7.54 ± 0.13) × 10^{-8}	0.75 ± 0.34	0.97 ± 0.02	–	0.609	0.99
PNI5	11,309.80 ± 180.43	(3.34 ± 0.08) × 10^{-7}	(3.36 ± 0.26) × 10^{-7}	3.31 ± 1.51	0.91 ± 0.02	1.55	0.557	0.98
PNI10	447.06 ± 9.97	(4.27 ± 0.09) × 10^{-6}	(3.19 ± 0.20) × 10^{-6}	3.35 ± 3.35	1.00 ± 0.06	0.14	0.344	0.96
PNI15	5246.40 ± 52.18	(9.10 ± 0.08) × 10^{-7}	(9.37 ± 0.43) × 10^{-7}	1.52 ± 0.99	1.00 ± 0.04	3.16	0.514	0.97
PNI20	26,764.00 ± 1382.45	(7.16 ± 0.42) × 10^{-8}	(7.5 ± 0.01) × 10^{-8}	1.98 ± 1.09	1.00 ± 0.03	2.82	0.560	0.97

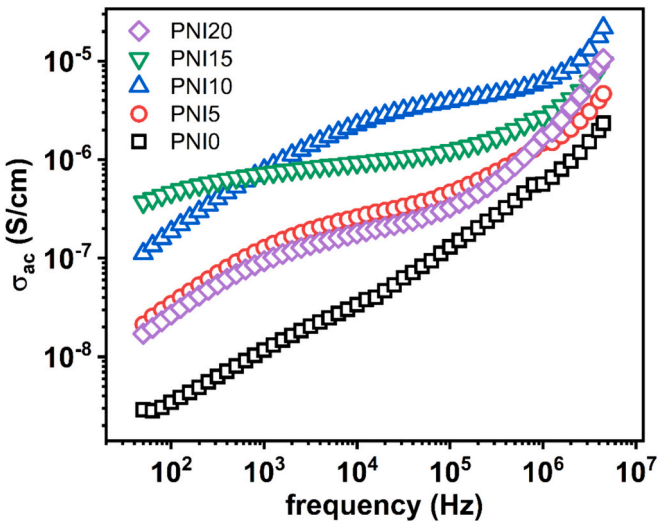

Fig. 8. AC conductivity of NaAlg/PVA-NaI SPEs as a function of frequency.

$C\omega^s$ which can be mathematically represented by Eq 17.

$$\sigma_{ac} = \sigma_{dc} + C\omega^s \tag{17}$$

In Eq (17), C is a constant and s is the exponent that determines the frequency dependence of the AC conductivity. The first term in the UPL is temperature-dependent. The second component of the equation is dependent on both frequency and temperature and pertains to the dielectric relaxation of the charge carriers within the material. This term captures the dynamic processes involved as the carriers interact with the surrounding lattice, thereby influencing the overall conductivity and dielectric properties of the material. Parameter s indicates the degree of interaction between the mobile ions and their surroundings. The value of s typically falls between 0 and 1, where 0 indicates no interaction, and 1 indicates a strong interaction. The exponent s is defined as in Eq (18).

$$s = \frac{\text{Backhop rate}}{\text{Site relaxation rate}} \tag{18}$$

In Eq 18, the numerator term is related to the backward hop of the carrier to its initial site. This hop occurs because of Coulomb repulsion between the mobile ions. When an ion hops to a new site, neighboring ions rearrange themselves to form a new potential minimum at the hopping ion site. This process is known as the site relaxation. The strength of the Coulomb interaction between mobile ions decreased as their concentration decreased. This decrease in the Coulomb interaction would reduce the back-hop rate, which is the rate at which an ion hops back to its original site.

The UPL denoted by eq. (17) was used to fit the ac spectra, disregarding the low-frequency dispersion region, and the parameters are tabulated in Table 3.

The values of DC conductivity closely match those of conductivity from Nyquist formalism. The parameter s ranged from 0.91 to 1.00. The condition $s \leq 1$ suggests that hopping motion encompasses translational motion in conjunction with abrupt hopping events, indicative of charge carriers moving over longer distances before hopping. Conversely, when $s > 1$, this implies that the motion is characterized by localized hopping, where charge carriers are confined to their immediate vicinity without extending beyond their local neighborhood [45]. Since the obtained values of s are ≤ 1, the motion of the mobile ions is translation with sudden hopping. The AC conductivity spectra at various temperatures were fitted with UPL in the temperature range of 303–363 K to evaluate the various conduction mechanisms. Four main models have been used to describe the behavior of the exponent "s" in ion hopping [46]. The quantum mechanical tunneling (QMT) model predicts that s will remain constant with temperature, whereas the small polaron tunneling (SPT) model predicts that s will increase with temperature. The Correlated Barrier Hopping (CBH) model proposes that the parameter s diminishes as the temperature increases, reflecting a transition in the hopping mechanism of charge carriers over potential barriers within the material. However, the overlapping large polaron quantum mechanical Tunneling (OLP) model anticipates that s will decrease with increasing temperature up to a certain point, at which it will reach a minimum value before starting to increase again, suggesting a change in the dominant conduction mechanism. Due to convergence issues with the Universal Power Law (UPL) fit at temperatures exceeding 363 K, the value of s was not determined beyond this temperature threshold, limiting the analysis to the thermal range where reliable data could be obtained. In our case, because the s value was 1 (Fig. 9b) within the given temperature range, the conduction mechanism obeyed the QMT model.

3.4.1. AC conductivity scaling

Scaling studies of experimentally measured quantities provide insights into the underlying reasons for the physical properties. The scaling procedure, referred to as the time-temperature superposition principle (TTSP), is used to investigate whether the conduction mechanism is influenced by temperature. With an increase in temperature, if the onset point of the conductivity dispersion shifts towards higher frequency values, it becomes feasible to scale the conductivity spectra across different temperatures. This scaling process can lead to the creation of a unified master curve that depicts the conductivity behavior across the entire temperature range. This approach efficiently consolidates the conductivity data, demonstrating the uniform alteration of the conductive properties of the material with temperature. *V*arious methods have been suggested for scaling the plots of AC conductivity [47]. In general, scaling is represented by Eq 19:

$$\frac{\sigma_{ac}(f)}{\sigma_{dc}} = F\left(\frac{f}{f^*}\right) \tag{19}$$

In Eq 19, F is the temperature and composition independent scaling factor, f^* is the scaling parameter for each conductivity isotherm. In the following case, f^* is taken as the hopping frequency f_p (frequency at which free hopping changes to correlated hopping), the frequency at which $\sigma_{ac}(f) = 2\sigma_{dc}$. Fig. 10 shows the scaling behavior of the conductivity data at different frequencies and temperatures for the PNI10 sample. The scaling plot collapses into a single "master curve", implying that the conductivity dispersion obeys the time-temperature superposition principle. The master curve illustrates that the shape of the curve remains consistent regardless of temperature variations. This demonstrates that the relaxation dynamics of charge carriers in the NaAlg-PVA-NaI polymer electrolytes adhere to a uniform mechanism at all temperatures [48].

3.5. Dielectric properties

The prepared biopolymer film contained various functional groups, including −OH and C═O, which were connected to the polymer structure. By analyzing the dielectric permittivity of the film, a deeper understanding of how polymer chains behave during relaxation and how functional groups react and adjust their orientation when exposed to an external electric field can be obtained [42]. Dielectric permittivity spectra can be used to observe the impact of polarization. Polar-polymer-based electrolytes exhibit diverse polarization mechanisms, such as ionic, dipolar, and electronic, when exposed to an external electric field. These mechanisms are influenced by the movement of ions within the polymer matrix, the orientation of polar groups, and the displacement of electrons and electron clouds, which contribute to the overall dielectric response of the material. [8]. The polymer electrolyte becomes polarized in the presence of an external electric field. The polarization (P) of the system is defined as $P = \frac{p}{V}$, where p represents the

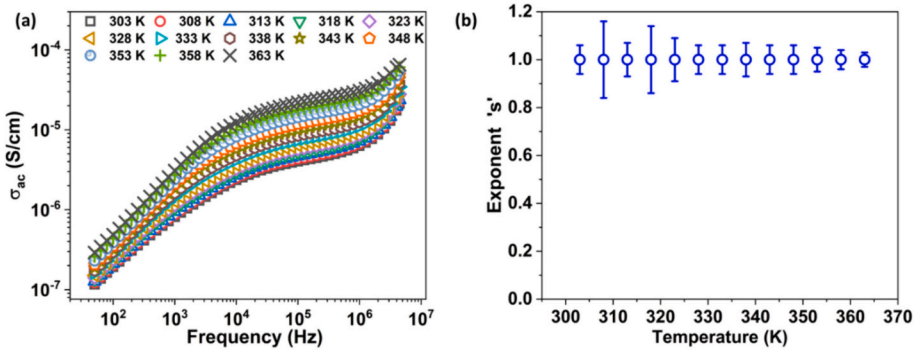

Fig. 9. (a) AC conductivity spectra for temperatures 303 K- 363 K and (b) exponent *s* for the PNI10 film at various temperatures.

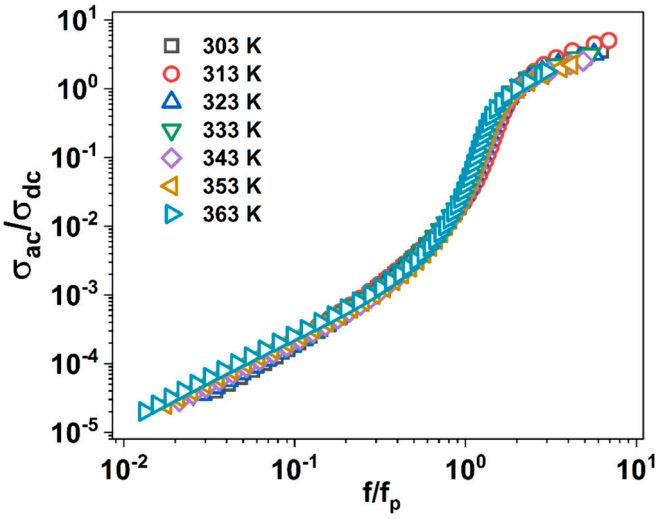

Fig. 10. AC conductivity scaling plots of PNI10 at different temperatures.

induced electric dipole moment, and *V* represents the volume.

The polarized polymer electrolyte system possesses a permanent electric dipole moment attributable to polar polymers, such as Polyvinyl Alcohol (PVA) and Sodium Alginate (NaAlg), along with an induced dipole moment that arises from the applied external electric field. In the linear approximation, the polarization (*P*) is directly proportional to the strength of the electric field (*E*) and can be expressed as $P = \varepsilon_o \chi E$. Here, ε_o represents the dielectric permittivity of free space, and χ is the dielectric susceptibility of the material. The dielectric permittivity is a complex quantity that can be expressed by eq. (20).

$$\varepsilon^*(\omega) = \varepsilon' - j\varepsilon'' = \frac{1}{j\omega C Z^*(\omega)} \tag{20}$$

In eq. (20), ε' is the real part and ε'' is the imaginary part of permittivity. The parameter $j = \sqrt{-1}$. Fig. 11(a) and (b) show the real and imaginary parts of the permittivity of the NaAlg-PVA-NaI SPEs, respectively. The PNI10 and PNI15 films exhibited the highest dielectric permittivity, suggesting that the inclusion of 10 wt% and 15 wt% salt in the biopolymer matrix generates a large number of free charge carriers at the electrode-electrolyte interface. Additionally, the low crystallinity of these samples allows for the maximum mobility of charge carriers, resulting in the highest conductivity values (the system's elevated

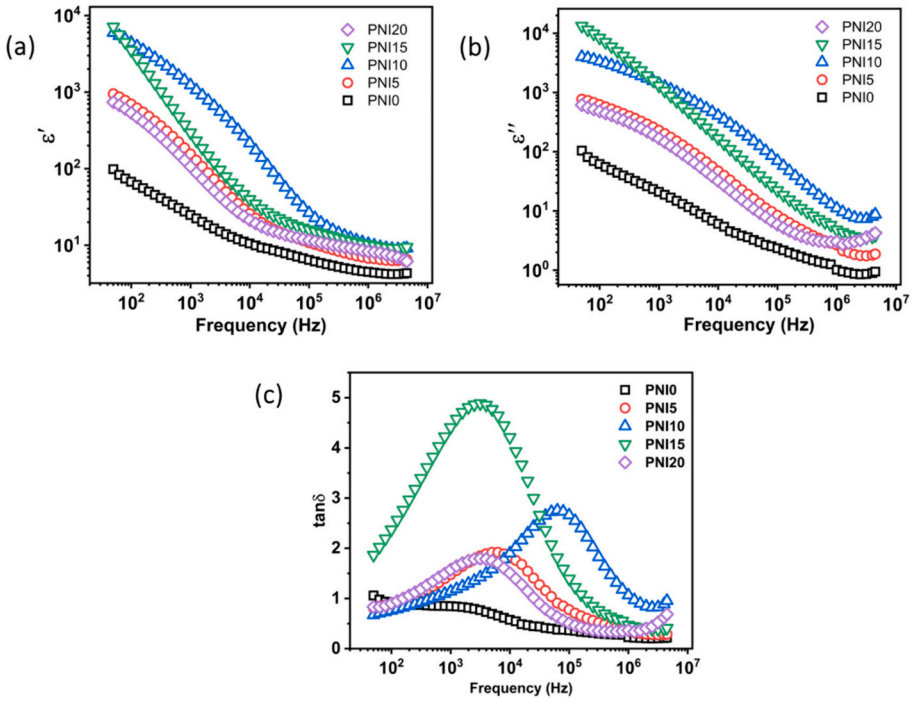

Fig. 11. Variation of (a) ε', (b) ε'' and (c) tan δ as a function of frequency at room temperature for NaAlg/PVA-NaI SPEs.

amorphous nature facilitates the concentration of free charge carriers at the interface between the electrode and electrolyte) [49]. The values of ε' and ε'' were high at low frequencies and decreased as the frequency increased. The high values of ε' and ε'' were due to the electrode polarization effect. Blocking electrodes prevent ions in the electrolyte from entering the external circuit, leading them to accumulate at the interface and resulting in polarization effects. The accumulation of polarizing ions at the interface increased the dielectric constant. At higher frequencies, the dielectric constant value decreases owing to rapid changes in the direction of the electric field, preventing the ions from aligning themselves quickly enough in the direction of the field. Consequently, there is no excess diffusion of ions in the direction of the field, and the accumulation of ions at the interface decreases, resulting in a reduction in the dielectric constant [50]. **Fig. 11**(c) shows a plot of the loss tangent as a function of frequency. Dielectric loss is the heat generated when AC is applied across the electrolytes. The energy from the AC voltage was absorbed by the electrolyte and converted to heat during the polarization process. The plot shows a single relaxation peak, indicating conductivity relaxation in the polymer chain. The relaxation time, τ is calculated using eq. (21).

$$\tau = \frac{1}{2\pi f_m} \tag{21}$$

In eq. (21), f_m is the frequency corresponding to maxima. This peak shifts to the right, implying that faster ion dynamics occur as the salt concentration increases to 10 wt%.

The dielectric properties are significantly affected by temperature. Fig. 12 illustrates the dielectric characteristics of the optimally conducting sample (PNI10) at various temperatures.

Typically, non-polar polymers exhibit temperature-independent ε' values, whereas strongly polar polymers show an increase in ε' with increasing temperature. The observed pattern of ε' in the current studies aligns with that of polar dielectrics, where higher temperatures promote dipole alignment, consequently leading to augmented dielectric permittivity [51]. It is clear from **Fig. 12**(a) and (b) that ε' and ε'' increase with temperature owing to the increase in the carrier concentration. This is because thermal energy is sufficient to dissociate the salt into Na^+ and I^- ions, leading to more free ions in the electrolyte, as supported by eq. (22).

$$n = n_o exp\left(-\frac{U}{k_b T}\right) \tag{22}$$

In Eq 22, n represents the free carrier density, U denotes the salt dissociation energy, k_b is the Boltzmann constant, and T is the temperature in Kelvin. Notably, no discernible relaxation peak was observed in the plot of ε'', suggesting the absence of primary or secondary structural relaxation phenomena within the polymer across the provided temperature range. The plot of the tangent loss for the selected temperature range indicates a single nonsymmetric peak of the conductivity relaxation. The deviation of the peak from the symmetric behavior indicates the non-Debye nature of relaxation. A peak shift to the right and an increase in peak area were observed. The shift in the peak indicated a reduction in the relaxation time. The increased peak width demonstrates an increase in carrier concentration with increasing temperature.

3.5.1. *Scaling of tangent loss spectra*

Scaling studies of experimentally measured quantities can provide insights into the underlying reasons for the physical properties. The scaling procedure, referred to as the time-temperature superposition principle (TTSP), is used to investigate whether the conduction mechanism is influenced by temperature. **Fig. 12**(d) shows the tangent loss of PNI10 plotted in scaled coordinates. i.e. $\frac{tan\delta}{tan\delta_{max}}$ plotted against $\frac{f}{f_{max}}$ for various temperatures, where f_{max} is the frequency corresponding to the maxima in tangent loss $tan\delta_{max}$. The entire dielectric loss data collapses into a single master curve, except at low frequencies. The deviation in the collapse of the graph at low frequencies was due to electrode polarization (EP). The scaling behavior of the tangent loss indicates that the conduction mechanism is independent of the temperature. That is, it follows the same mechanism within a given temperature range [52].

3.6. *Modulus spectrum*

The complex electric modulus, which is the inverse of the complex permittivity, could offer a deeper understanding of the conductivity relaxation in the SPE system. **Fig. 13**(a) and (b) show the real and imaginary parts of the complex modulus, respectively. The M' and M''

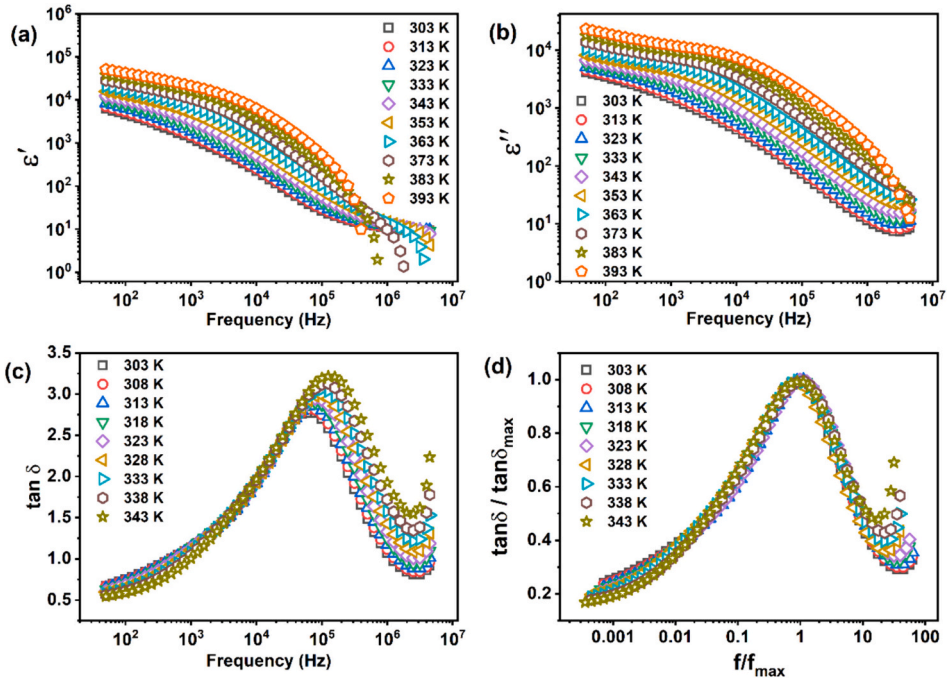

Fig. 12. Variation of (a) ε', (b) ε'', (c) tan δ and (d) scaling of tangent loss for PNI10 at selected temperatures.

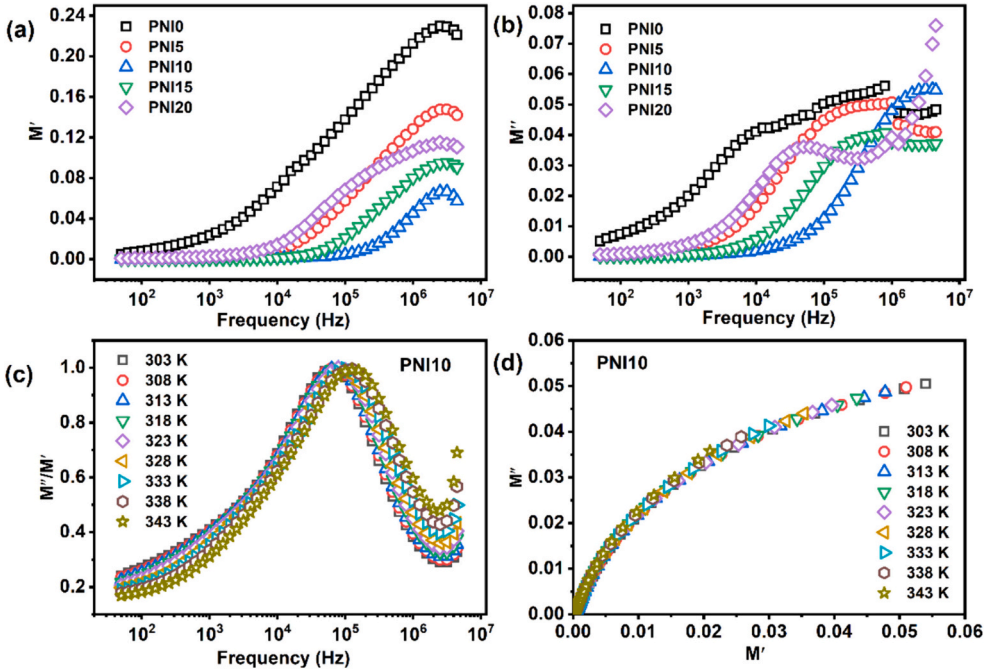

Fig. 13. Variation in (a) M' and (b) M'' for NaAlg/PVA-NaI SPEs. Variation of (c) normalized plot of modulus and (d) Argand diagram for PNI10 sample at the selected temperature.

spectra exhibited long tails at low frequencies, suggesting that the electrode polarization effect (EP) had a minimal contribution. The presence of electrode polarization (EP) effect results in a low value of M' in the low-frequency region as $M^*(\omega) = \frac{1}{\varepsilon^*(\omega)}$. As the frequency increases, the value of M' gradually increases. The dispersion observed in the electric-modulus spectra is attributed to the relaxation of conductivity over a wide range of frequencies. At higher temperatures, the M'' spectra peak moved towards a higher frequency owing to salt incorporation and hence an increase in the amorphousness of the PNI10 sample. In addition, the appearance of relaxation peaks that were asymmetric in nature in M''spectra for SPE films indicated a relaxation behavior that was not of the Debye type (single relaxation time) [53].

Fig. 13(c) presents the variation of normalized $\frac{M'}{M}$ spectra at specific temperatures for the PNI10 electrolyte. The plot shows a long tail at low frequencies due to the large capacitance of the electrodes. The shape of the spectrum remained the same as the temperature increased; nevertheless, the peak maximum shifted towards higher frequencies. This shift indicates that the relaxation process was thermally activated, signifying the occurrence of charge-carrier hopping within the system [54]. The asymmetric nature of $\frac{M'}{M}$ curve implies that the conductivity relaxation is non-exponential and can be described by the Kohlrausch–Williams–Watts (KWW) function $\phi(t)$. This function represents the distribution of the relation times in polymer electrolytes. The dielectric modulus is given by eq. (23):

$$M^* = M_\infty \left[1 - \int_0^\infty e^{-i\omega t}\left(\frac{d\phi}{dt}\right)dt\right] \tag{23}$$

$$\phi(t) = e^{\left(-\frac{t}{\tau_\infty}\right)^\beta} \tag{24}$$

In Eq 24, τ_∞ and β are the conductivity relaxation time and KWW exponent. The β value corresponding to the PNI10 samples from 303 K to 343 K was in the range of 0.56 and 0.62. A value of $\beta < 1$ indicates a non-Debye nature of relaxation [55]. In this study, the Argand plots (Fig. 13 (d)) reveal incomplete semi-circular arcs, indicating the existence of a distribution of relaxation times, which signifies non-Debye properties. This suggests that ion transport within this system predominantly occurs through viscoelastic relaxation.

3.7. Transport properties of charge carriers

The ion transport parameters, such as carrier concentration (n), diffusion coefficient (D), and mobility (μ), were obtained by fitting the Nyquist plot with eqs. (13) and (14) derived from EEC [44]. From the fitting, parameters such as k_2, ε_r, τ_2 and σ was substituted into Eq 25, 26 and 27 to estimate the values of transport parameters.

$$D = \frac{e(k_2\varepsilon_r\varepsilon_o A)^2}{\tau_2} \tag{25}$$

$$\mu = \frac{eD}{k_b T} \tag{26}$$

$$n = \frac{\sigma}{\mu e} \tag{27}$$

The variations in n, μ, and D for NaAlg/PVA at various NaI concentrations are shown in Fig. 14. The room temperature conductivity (25 °C) of the NaAlg/PVA-NaI electrolytes increased with salt inclusion and reached an optimum value of 4.42×10^{-6} S cm^{-1} (PNI10 electrolyte). The conductivity decreased with increasing salt concentration above 10 wt%. Clearly, the charge carrier concentration followed a conductivity trend. The mobility and diffusion coefficient of the charge carriers followed an inverse conductivity trend. Thus, it can be concluded that the carrier concentration mainly influences the conductivity rather than the mobility and diffusion coefficient. Because of the high carrier concentration in the PNI10 and PNI15 samples, the mobility and diffusion coefficient were reduced owing to the lowering of the space available for free ion migration. Because of the ion association in the PNI20 sample, the carrier concentration was significantly reduced, leading to a large decrease in the ionic conductivity.

The transport properties of the prepared samples were analyzed in the temperature range 303 K–363 K and are presented in Fig. 15. To investigate the rise and fall in ionic conductivity, Nyquist plots across a range of temperatures were used to evaluate and gauge the density of

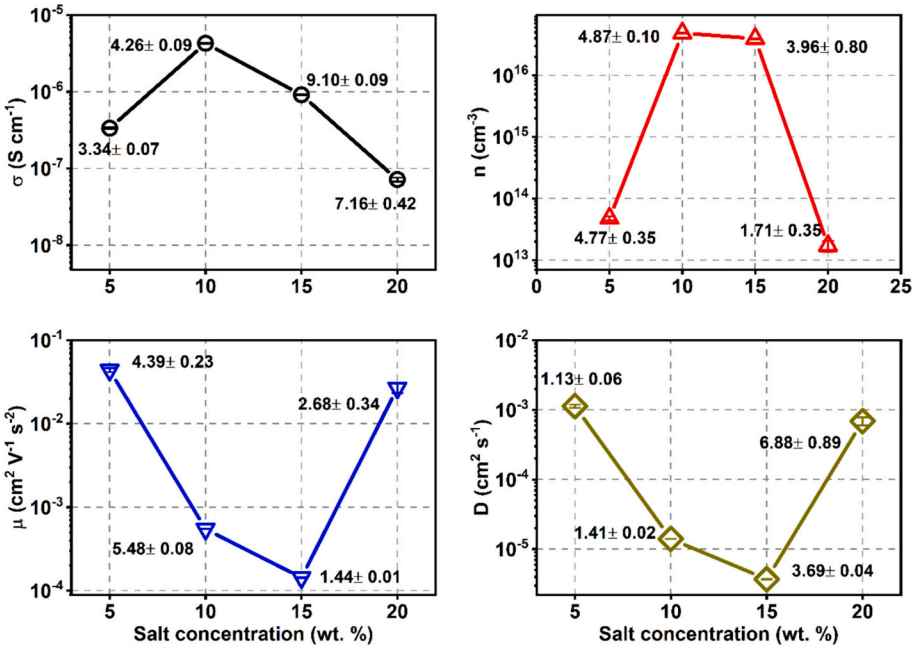

Fig. 14. Variation in transport parameters for NaAlg/PVA with different NaI salt concentrations.

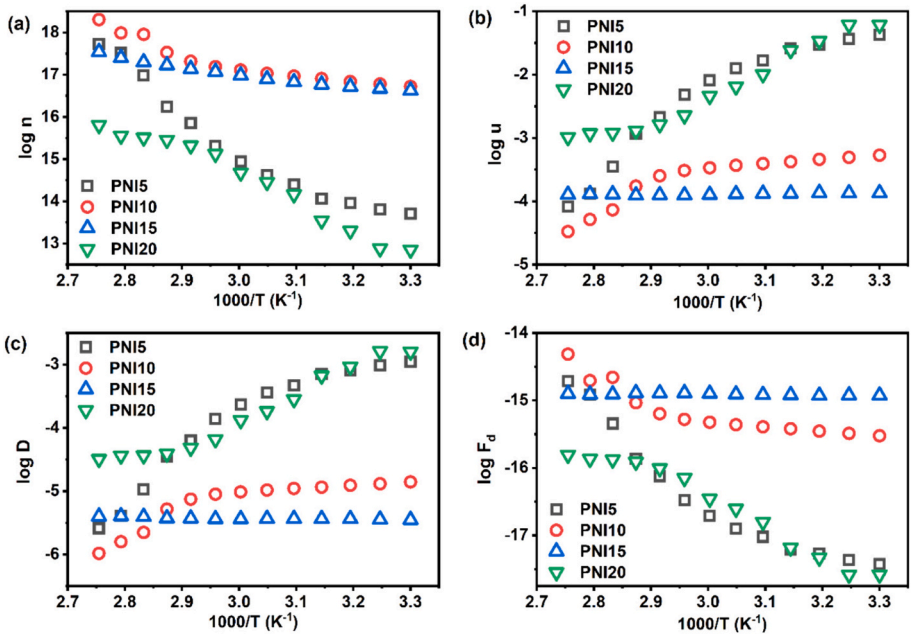

Fig. 15. Variation of high temperature transport parameters (a) number density, n, (b) mobility, μ, (c) diffusion coefficient, D and (d) drag coefficient, F_d for NaAlg/PVA-NaI SPEs.

charge carriers, their mobility, and diffusivity. As the temperature increases, there is a corresponding increase in the charge carrier density. This is because of the additional energy supplied at higher temperatures, which is sufficient to break the ionic bonds, resulting in the formation of free ions. This process accounts for the observed increase in charge-carrier density within the system. The highest conducting sample, PNI10, had the highest carrier density at the studied temperatures owing to its highly amorphous nature [23]. Consequently, the increase in carrier concentration led to reduced mobility and diffusion coefficients, primarily owing to the heightened ion collisions caused by the limited space available for carrier movement. Upon applying an electric field across the sample, the ions begin to move randomly within the confined space, leading to an increase in the number of ion collisions.

This scenario results in a slower movement of ions, thereby decreasing the mobility and diffusivity of the charge carriers. This decrease in both the number of charge carriers (n) and mobility (μ) was consistently observed across all the samples [56]. The variation in the Stokes drag coefficient F_d is depicted as a function of temperature. The Stokes drag coefficient increased with increasing temperature. This coefficient is closely related to the level of amorphousness and viscosity within the polymer matrix. An increase in the Stokes drag coefficient signifies an increase in viscosity, leading to a deceleration in the motion of charge carriers within the system. The ionic conductivity of the highest conducting sample at elevated temperatures followed the same

trend as that of the carrier concentration, implying the direct influence of n on σ.

3.8. Thermal studies

The thermal stability of a polymer electrolyte is a critical parameter governing the operational temperature range of the device. Fig. 16 shows the TGA and DTG curves of the prepared electrolyte samples. There were three decomposition steps. The first step (RT – 100 °C) involved the elimination of moisture from the sample. Because the samples were dried in a hot air oven and stored in desiccators, this mass loss was due to the moisture occluded while handling the sample. The second step (200–300 °C) is related to the decomposition of $-CO_2$ due to the decarboxylation process and the breakage of the glycosidic linkage of NaAlg and decomposition of −OH groups, leading to a mass loss of approximately 45%, indicating major mass decomposition [57,58]. The third step was observed due to the decomposition of the remaining carbon residues, without any residue remaining at the end of the experiment. The maximum decomposition temperatures with the corresponding mass losses are presented in Table 4. As listed in Table 4, the prepared samples underwent a drastic mass loss above 200 °C, which is significantly higher than the operating temperature of any electrochemical device. Furthermore, the inclusion of salt led to a minor reduction in the thermal stability of the optimal sample (PNI10), which was attributed to weakening of the glycosidic linkage within the polymer matrix. Although there was a slight decrease in the decomposition temperature of the PNI10 sample, this was not very prominent. The PNI10 sample is still considered the most suitable for use as a charge-transport medium in electrochemical device applications.

To observe the shift in the glass transition temperature (T_g) resulting from the blending of the two polymers with its incorporation salt, differential scanning calorimetry (DSC) was conducted. The DSC thermograms for the NaAlg/PVA-NaI SPEs are shown in Fig. 17, and the *Tg* values for each electrolyte are listed in Table 4. The DSC thermogram exhibited two prominent regions. The first endothermic peak in the RT-150 °C region indicates dehydration of the sample. The step transition in this region signifies the T_g. The second region consists of an endothermic peak (around 200 °C) followed by an exothermic peak (around 240 °C) attributed to the decomposition of the polymer, resulting in a carbonized residue, in agreement with the TGA results [58]. A single T_g was observed for the pure blend and the salt-doped blend, indicating the compatibility of the blends even after doping [59]. Initially, the T_g increased to 10 wt% of salt concentration. A further increase in the salt

Table 4
Thermal parameters extracted from TGA and DTG graphs of NaAlg/PVA-NaI SPEs.

Sample	Glass transition temperature, T_g (°C)	Maximum decomposition temperature, T_d (°C)	Percentage of mass loss (%)
PNI0	52.5	223.96	39.93
PNI5	85.2	222.54	60.79
PNI10	91.6	218.54	46.08
PNI15	79.7	227.25	45.85
PNI20	65.4	219.97	52.23

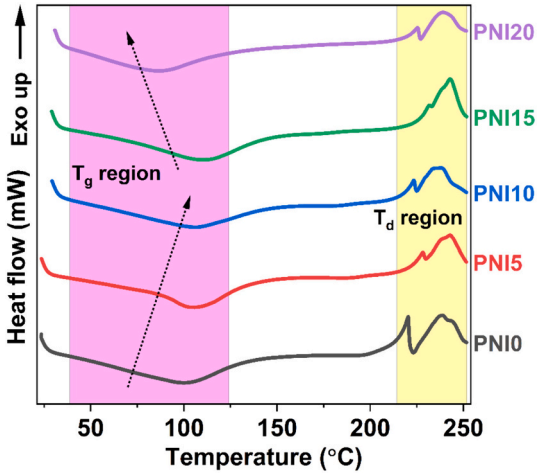

Fig. 17. DSC thermograms of NaAlg/PVA-NaI SPEs.

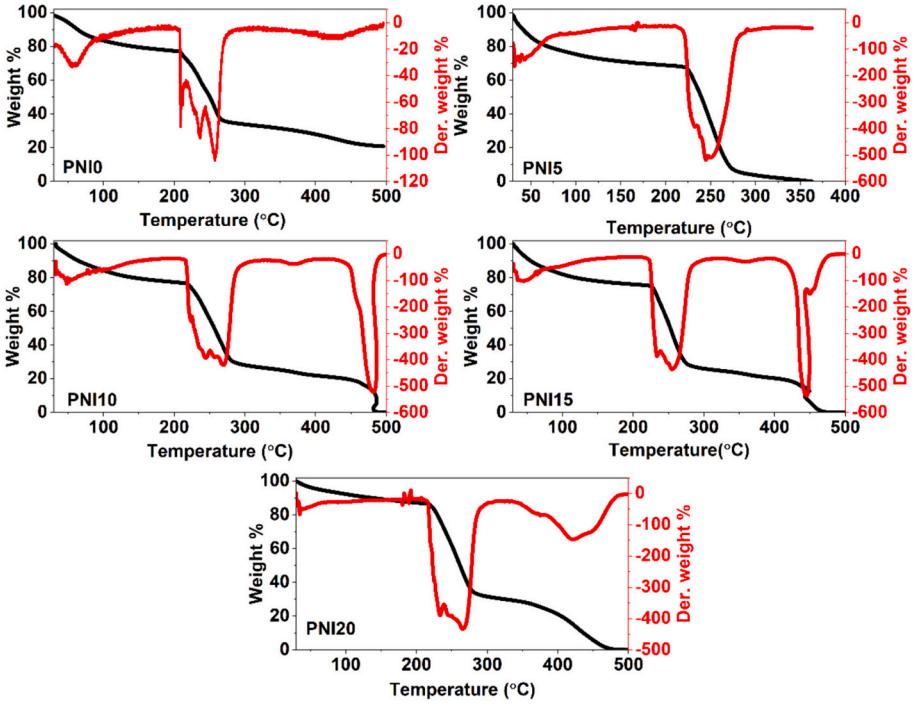

Fig. 16. TGA and DTG curves of NaAlg/PVA-NaI SPEs.

concentration decreases T_g. This can be attributed to the 'transient crosslinks' that occur due to the interaction of the salt cation (Na^+) with the −OH groups of the polymer blend. The probability of crosslinking is directly related to the carrier concentration. Since the carrier concentration is the highest for PNI10, T_g is the highest for this sample and decreases with further increase in salt concentration. Similar variations were reported in our earlier work [39,60].

3.9. Morphological studies

Surface morphology plays a role in determining the overall ion transport across the electrode-electrolyte interface. The surface texture was examined using SEM, and the images are shown in Fig. 18. The pure blend exhibited a smooth morphology without any pores, indicating excellent compatibility between PVA and NaAlg polymers. Small micropores were observed upon the incorporation of the NaI salt. The porosity of the electrolyte directly affects its ionic conductivity because the connectivity of the pores is crucial for facilitating the movement of charge carriers through the electrolyte [61]. A porous structure allows ions to migrate easily with minimal hindrance. This can be attributed to the increased surface area provided by the pores, which facilitates ion diffusion and enhances their transport through the material. For PNI15, the pores exhibited significant enlargement and amalgamation, suggesting the highest level of amorphousness among all doped samples. [62–64]. For the PNI15 and PNI20 samples, a porous structure was not observed. Instead, hexagonal structures with thick barriers or island-like

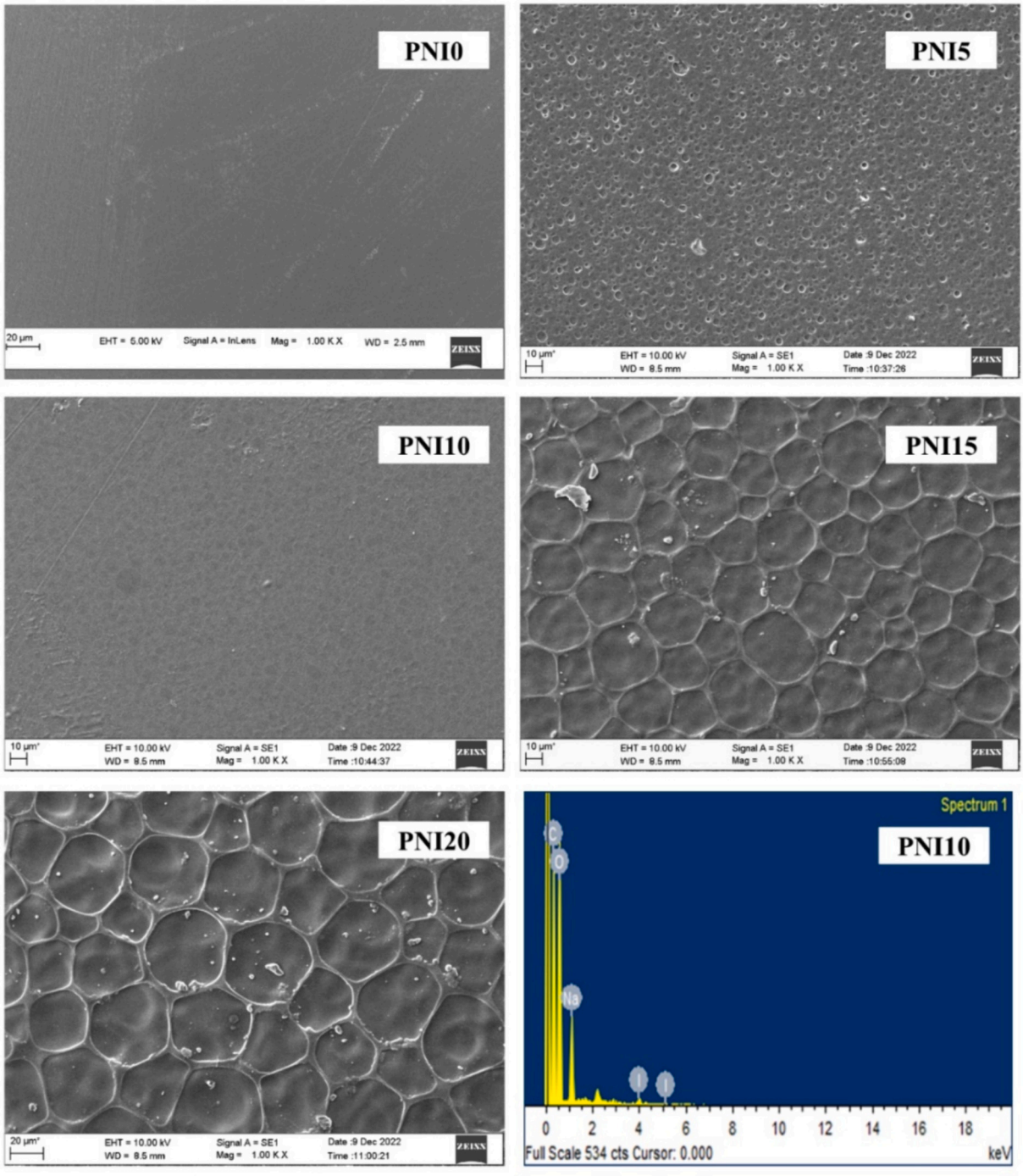

Fig. 18. SEM images of NaAlg/PVA–NaI SPEs. EDAX spectra of the highest conducting sample-PNI10 (bottom right corner).

structures are mostly visible, which hinders ion conduction [65]. In addition, white patches were observed, which may indicate the onset of ion aggregation in the sample, leading to an overall decrease in the ionic conductivity of the sample. Fig. 18 shows the EDAX spectra of the PNI10 electrolyte, which had the highest conductivity. The spectra show the presence of characteristic atoms, including Na, C, and I, which were attributed to the NaAlg-PVA-NaI membrane. This suggests that the sample had a uniform composition.

3.10. Atomic Force microscopy

The surface morphologies of the prepared polymer blend electrolytes PNI0, PNI10, and PNI15 were examined by AFM (Fig. 19), where the tip was operated in the tapping mode in a scanning area of 5 μm × 5 μm. It is observed that the pure blend PNI0 has a root mean square (RMS) roughness of 11.5 nm. Incorporating 10 wt% NaI has led to a reduction in the surface roughness of PNI0, consequently diminishing the crystallinity of the blended polymer electrolyte and resulting in a smoother surface. This smoother surface facilitates faster ion conduction within the electrolyte [66]. The roughness of PNI10 reduced to 9.45 nm indicating a smoother morphology. Enhancing the uniformity of the surface can potentially improve the contact between the electrode and the electrolyte, leading to improved device performance [67]. Referring to transport analysis, the factor p_2 indicate the deviation of the spike from the ideal behavior ($p_2 = 1$). The closeness of the value of p_2 towards unity is an indication of the smoothness of the sample. The value of p_2 for PNI10 sample was 0.749 and for PNI15 was 0.734, indicating that PNI10 is smoother compared to PNI15. A further increase in the salt concentration increased the roughness to 13.9 nm, as observed in PNI15. This agrees with the SEM and XRD results, where further addition of the salt led to the onset of salt aggregation.

3.11. LSV and TNM studies

Determining the maximum operational voltage, also known as the electrochemical stability window (ESW), of a polymer electrolyte is crucial for evaluating its suitability for use in electrochemical devices [68]. For linear sweep voltammetry (LSV) measurements, the electrolytes were placed between sodium metal and inert planar electrodes such as Pt or stainless steel (SS). Inert working electrodes were employed to prevent unwanted reactions and interference with the background currents. In this case, the inert electrode was SS. The asymmetric cell was subjected to a voltage range of 0–5.5 V at a scan rate of 5 mV s^{-1}, and the LSV plot is shown in Fig. 20. The characteristic curve

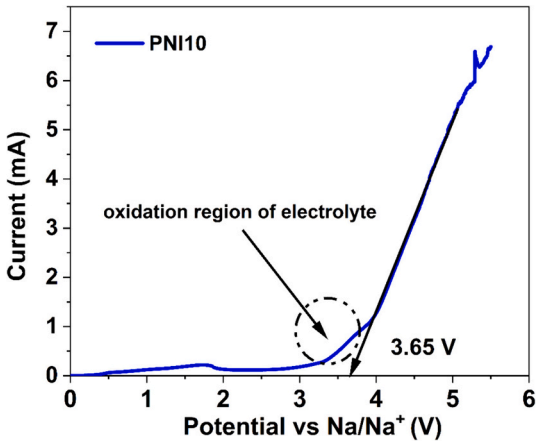

Fig. 20. LSV data for the PNI10 electrolyte.

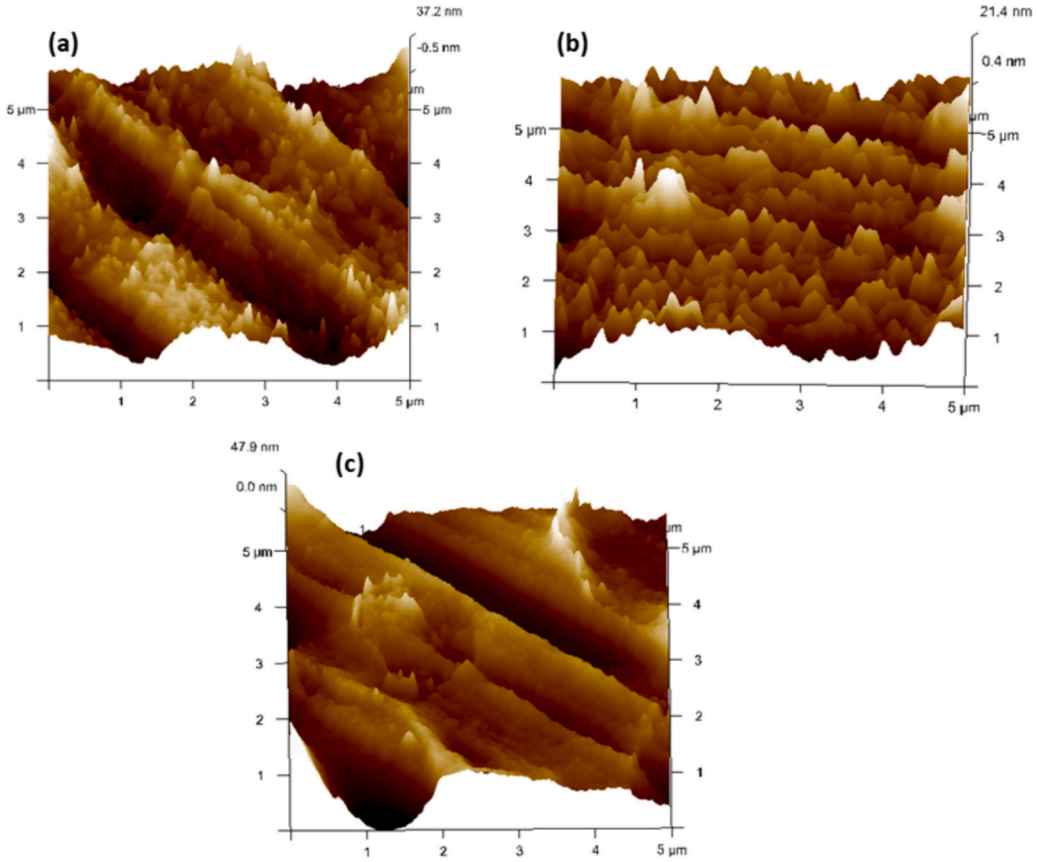

Fig. 19. 3D AFM images of (a) PNI0, (b) PNI10, and (c) PNI15 electrolytes.

demonstrates that the anodic current remained relatively constant within the voltage range of 0–3.65 V. However, beyond this range, a sudden surge in current was observed, which was attributed to ion decomposition at the electrode-electrolyte interface. This critical voltage, where ion decomposition is initiated, is termed the decomposition voltage of the electrolyte and is identifiable on the voltage axis where the current undergoes rapid escalation [69]. As shown in the figure, the PNI10 sample can maintain stability within the voltage range of 3.65 V, rendering it suitable for the fabrication of electrochemical (EC) devices.

In polymer electrolytes, both electrons and ions play important roles in ion conduction. For potential utility in electrochemical devices, an electrolyte must fulfil various criteria, including high room-temperature ionic conductivity, ionic transference number near unity, and minimal electronic conductivity [70]. The mobility of the ionic species is a critical factor in the design of new polymer electrolytes for batteries. The non-unity transference number of sodium ions in polymer electrolytes can lead to the formation of concentration gradients, causing the current to decay to lower steady-state values. Therefore, evaluation of polymer electrolytes must consider both the transference number and ionic conductivity [71]. The nature of charges, whether ions or electrons, can be determined by measuring the ionic transference number (TNM) using Wagner's polarization method [24]. To create a cell assembly for measuring the ionic transference number, the samples were placed between two stainless steel (SS) electrodes that acted as blocking electrodes, preventing the ions near the interface from polarizing while permitting the movement of electrons through the outer circuit [72]. Fig. 21 shows a plot of current versus time for the samples subjected to an applied DC polarization voltage of 100 mV. The total ionic and electronic transference numbers were calculated using Eq 6 and 7. Eqs. (8) and (9) were used to calculate the ionic and electronic conductivities by utilizing the ion-electron transference number and electrolyte bulk conductivity (σ) obtained from the EIS measurements. The values are listed in Table 5.

When the total ionic transference number is close to 1, the ions are the primary charge carriers. As a result, the ionic current is at its maximum, whereas the electronic current is at its minimum. This satisfies the requirements of energy storage devices.

3.12. Mechanical properties

During the process of bringing a battery or any energy-storage device to the market, an important factor to consider is its mechanical stability. In addition to possessing a high transference number and ionic conductivity, the polymer electrolyte must have mechanical properties that are sufficient to ensure long-term cycle stability. The stress-strain curve was examined to evaluate its mechanical stability. This is particularly crucial because during cell packaging, the polymer electrolyte is positioned between two electrodes and must withstand the applied pressure. If the polymer electrolyte lacks mechanical strength, it could lead to short-circuiting of the electrodes during the cell operation. Therefore, it is essential for the material to be inherently flexible and to avoid brittleness. It should possess inherent characteristics that enable it to absorb minor internal shocks without affecting electrodes. Mechanical strength is crucial because it directly affects dendrite suppression/resistance, leading to enhanced safety [73]. This is one of the primary benefits of polymer electrolytes over conventional polyolefin separators. Mechanical strength in the range 10^6–10^8 MPa is crucial for suppressing dendrite formation in typical solid-state lithium batteries [74]. Numerous metrics are available to assess mechanical properties, although the most prevalent metric discussed here is the tensile test. The compact polymer network, which enhances mechanical robustness, also limits polymer mobility, leading to reduced ionic mobility. This makes it challenging to simultaneously achieve an elevated ionic conductivity and tensile strength [73].

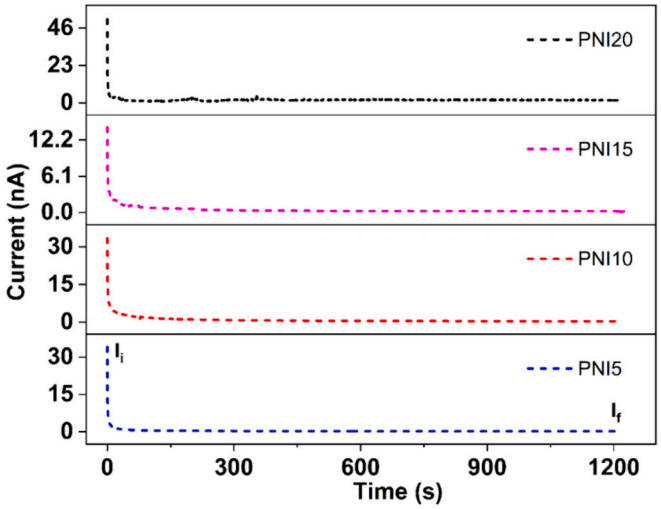

Fig. 21. TNM plot of NaAlg/PVA-NaI SPEs.

Table 5
Variation of t_{ion}, t_{elec}, σ_{ion}, and $\sigma_{electronic}$ of NaAlg/PVA − NaI samples.

Sample	t_{ion}	t_{elec}	σ_{ion} (S cm^{-1})	$\sigma_{electronic}$ (S cm^{-1})
PNI5	0.993	0.007	3.64×10^{-7}	2.56×10^{-9}
PNI10	0.991	0.009	4.38×10^{-6}	3.98×10^{-8}
PNI15	0.988	0.012	9.95×10^{-7}	1.21×10^{-8}
PNI20	0.969	0.031	7.68×10^{-8}	2.43×10^{-9}

The mechanical properties of solid polymer electrolytes (SPEs), including tensile strength, elongation at break, and Young's modulus, were determined by analyzing the stress–strain curves. The Young's modulus was computed by evaluating the slope of the linear segment of the stress–strain curve. The tensile strength was derived from the maximum stress point on the curve, whereas the elongation at break was obtained from the strain axis limit. Fig. 22 depicts the stress-strain curve and variations in parameters such as tensile strength, Young's modulus, and elongation at break with varying salt concentrations. Table 6 lists the parameter values obtained for each sample.

Creating a standard for the tensile strength of Na-based SPEs is difficult because of the wide range of strengths observed, which typically fall between 1.5 and 40 MPa [75–78]. However, based on the results obtained in Table 6, the tensile strength of SPEs ranges from 21 to 45 MPa, which is quite high for polymer-based electrolytes. Additionally, **Fig. 22**(b) indicates that the tensile strength is not significantly affected by the salt used.

3.13. Biodegradability test

To prevent environmental contamination, the prepared solid electrolyte material must decompose under atmospheric conditions [26]. Two primary degradation mechanisms were observed during the soil burial tests. Initially, the film surface undergoes swelling owing to the adsorption of water molecules, thereby creating a favorable environment for microbial proliferation. Subsequently, enzymatic degradation occurs as microbes commence the breakdown of the polymeric chain [79]. Owing to the adhesive properties of the NaCMC-PVA polymer, soil adheres to the film surface, posing challenges in accurately determining the final weight of the film [33]. However, the sample exhibited slow degradation, as shown in **Fig. 23**(a)–(d). Thus, the degradation of the polymer was confirmed.

4. Conclusion

Sodium ion-conducting polymer blend electrolytes based on NaAlg

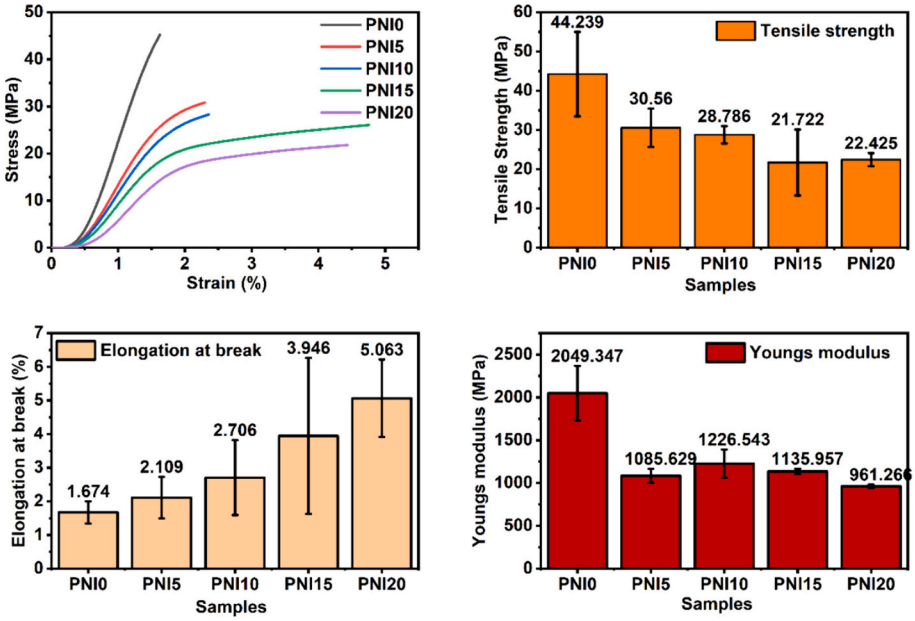

Fig. 22. (a) Tensile stress-strain curve and plot of (b) tensile strength, (c) Young's modulus, and (d) elongation at break for the prepared SPEs.

Table 6
Properties obtained from stress-strain curve of NaAlg/PVA-NaI SPEs.

Sample	Tensile strength (MPa)	Elongation at break (%)	Young's modulus (MPa)
PNI0	44.24 ± 10.75	1.67 ± 0.33	2049.35 ± 319.73
PNI5	30.56 ± 4.88	2.11 ± 0.62	1085.63 ± 81.00
PNI10	28.79 ± 2.21	2.71 ± 1.11	1226.54 ± 164.42
PNI15	21.72 ± 8.40	3.95 ± 2.32	1135.96 ± 31.06
PNI20	22.43 ± 1.65	5.06 ± 1.15	961.27 ± 19.88

and PVA were successfully synthesized using a facile solution casting technique. A maximum ionic conductivity of $(4.27 \pm 0.09) \times 10^{-6}$ S cm^{-1} was achieved at 298 K for the sample containing 10 wt% of NaI salt. The enhancement in the sample conductivity was substantiated by XRD, SEM, and EIS characterizations. The conduction mechanism for highest conducting electrolyte sample was elucidated using a Quantum Mechanical Tunneling (QMT) model. The increase in ionic conductivity upon the addition of NaI was linked to an increase in the carrier concentration of the ions. The dielectric behavior of the PNI10 sample exhibited a pronounced dependence on both frequency and

Fig. 23. Highest conducting electrolyte (PNI10) undergoing degradation at various time intervals.

temperature, demonstrating a non-Debye-type dielectric relaxation. The incomplete semicircular arc observed in the Argand plots further confirms the non-Debye nature of the relaxation process, suggesting that ion transport occurs through the viscoelastic relaxation process. Despite possessing adequate electrochemical stability and mechanical strength, the optimally conducting sample falls short of achieving high ionic conductivity ($<10^{-4}$ S cm^{-1}), rendering it unsuitable for applications in energy storage devices. Therefore, it is imperative to enhance conductivity by integrating nanofillers or plasticizers into an optimally conducting sample to meet technological requirements.

CRediT authorship contribution statement

Vipin Cyriac: Writing – original draft, Methodology, Investigation, Formal analysis, Data curation, Conceptualization. **Ismayil:** Writing – review & editing, Validation, Supervision, Resources. **Kuldeep Mishra:** Validation, Resources, Data curation. **Y.N. Sudhakar:** Writing – review & editing, Validation, Resources, Data curation. **Z.E. Rojudi:** Formal analysis, Data curation. **Saraswati P. Masti:** Data curation. **I.M. Noor:** Writing – review & editing, Validation, Resources.

Declaration of competing interest

The authors declare that they have no known competing financial interests or personal relationships that could have appeared to influence the work reported in this paper.

Data availability

Data will be made available on request.

Acknowledgements

One of the authors, Vipin Cyriac, acknowledges the support received from the Directorate of Minorities, Bengaluru, the Government of Karnataka, India. Financial assistance in the form of the Directorate of Minorities Fellowship for Minority Students, as per the sanction order DOM/Fellowship/CR-10/2019-20 dated 29-06-2020, is gratefully acknowledged for facilitating this research.

References

[1] D.E. Fenton, J.M. Parker, P.V. Wright, Complexes of alkali metal ions with poly (ethylene oxide), Polymer (Guildf) 14 (1973) 589, https://doi.org/10.1016/0032-3861(73)90146-8.
[2] T.S. Bhat, P.S. Patil, R.B. Rakhi, Recent trends in electrolytes for supercapacitors, J. Energy Storage 50 (2022) 104222, https://doi.org/10.1016/J.EST.2022.104222.
[3] Y. Wang, K.S. Chen, J. Mishler, S.C. Cho, X.C. Adroher, A review of polymer electrolyte membrane fuel cells: technology, applications, and needs on fundamental research, Appl. Energy 88 (2011) 981–1007, https://doi.org/10.1016/J.APENERGY.2010.09.030.
[4] M.S. Su'ait, M.Y.A. Rahman, A. Ahmad, Review on polymer electrolyte in dye-sensitized solar cells (DSSCs), Sol. Energy 115 (2015) 452–470, https://doi.org/10.1016/J.SOLENER.2015.02.043.
[5] S. Muench, A. Wild, C. Friebe, B. Häupler, T. Janoschka, U.S. Schubert, Polymer-based organic batteries, Chem. Rev. 116 (2016) 9438–9484, https://doi.org/10.1021/ACS.CHEMREV.6B00070/ASSET/IMAGES/LARGE/CR-2016-00070V_0020.JPEG.
[6] F. Opekar, K. Štulík, Electrochemical sensors with solid polymer electrolytes, Anal. Chim. Acta 385 (1999) 151–162, https://doi.org/10.1016/S0003-2670(98)00583-2.
[7] K.S. Ngai, S. Ramesh, K. Ramesh, J.C. Juan, A review of polymer electrolytes: fundamental, approaches and applications, Ionics (Kiel) 22 (2016) 1259–1279, https://doi.org/10.1007/s11581-016-1756-4.
[8] S.B. Aziz, T.J. Woo, M.F.Z. Kadir, H.M. Ahmed, A conceptual review on polymer electrolytes and ion transport models, J. Sci. Adv. Mater. Dev. 3 (2018) 1–17, https://doi.org/10.1016/j.jsamd.2018.01.002.
[9] R. Chen, W. Qu, X. Guo, L. Li, F. Wu, The pursuit of solid-state electrolytes for lithium batteries: from comprehensive insight to emerging horizons, Mater. Horiz. 3 (2016) 487–516, https://doi.org/10.1039/C6MH00218H.
[10] J.W. Fergus, Ceramic and polymeric solid electrolytes for lithium-ion batteries, J. Power Sources 195 (2010) 4554–4569, https://doi.org/10.1016/J.JPOWSOUR.2010.01.076.
[11] N.F. Mazuki, A.F. Fuzlin, M.A. Saadiah, A.S. Samsudin, An investigation on the abnormal trend of the conductivity properties of CMC/PVA-doped NH4Cl-based solid biopolymer electrolyte system, Ionics (Kiel) 25 (2019) 2657–2667, https://doi.org/10.1007/s11581-018-2734-9.
[12] P.R. Hari, T. Chandy, C.P. Sharma, Chitosan/Calcium-Alginate Beads for Oral Delivery of Insulin, (n.d.). https://doi.org/10.1002/(SICI)1097-4628(19960314)59:11.
[13] T. Çaykara, S. Demirci, Preparation and characterization of blend films of poly (vinyl alcohol) and sodium alginate 43 (2007) 1113–1121, https://doi.org/10.1080/10601320600740389.
[14] T. Sheela, R.F. Bhajantri, P.M.G. Nambissan, V. Ravindrachary, B. Lobo, J. Naik, S. G. Rathod, Ionic conductivity and free volume related microstructural properties of LiClO4/PVA/NaAlg polymer composites: positron annihilation spectroscopic studies, J. Non-Cryst. Solids 454 (2016) 19–30, https://doi.org/10.1016/J.JNONCRYSOL.2016.10.010.
[15] T. Sheela, R.F. Bhajantri, V. Ravindrachary, P.K. Pujari, S.G. Rathod, Preparation and characterization of NaClO4 doped poly(vinyl alcohol)/sodium alginate composite electrolyte, in: AIP Conf Proc, American Institute of PhysicsAIP, Department of Physics, Mangalore University, Mangalagangotri - 574 199, India, 2013, pp. 1302–1303, https://doi.org/10.1063/1.4791531.
[16] T. Sheela, R.F. Bhajantri, V. Ravindrachary, P.K. Pujari, S.G. Rathod, J. Naik, Ionic conductivity studies in crystalline PVA/NaAlg polymer blend electrolyte doped with alkali salt KCl, AIP Conf. Proc. 1591 (2015) 202, https://doi.org/10.1063/1.4872544.
[17] A.F. Fuzlin, M.A. Saadiah, Y. Yao, Y. Nagao, A.S. Samsudin, Enhancing proton conductivity of sodium alginate doped with glycolic acid in bio-based polymer electrolytes system, J. Polym. Res. 27 (2020) 1–16, https://doi.org/10.1007/S10965-020-02142-0/FIGURES/6.
[18] R. Jansi, S. Shenbagavalli, M.S. Revathy, S. Deepalakshmi, P. Indumathi, M.K. A. Mohammed, Structural and ionic transport in biopolymer electrolyte-based PVA: NaAlg with NH4Cl for electrochemical applications, J. Mater. Sci. Mater. Electron. 34 (2023) 1–15, https://doi.org/10.1007/S10854-023-10302-3/FIGURES/13.
[19] R. Jansi, S. Shenbagavalli, M.S. Revathy, S. Deepalakshmi, Solid polymer electrolytes from NaAlg: PVA: effect of ammonium thiocyanate on ionic conductivity, J. Mater. Sci. Mater. Electron. 34 (2023) 1–13, https://doi.org/10.1007/S10854-023-09825-6/FIGURES/12.
[20] X. Shen, W. Xu, J. Xu, G. Liang, H. Yang, M. Yao, Quasi-solid-state dye-sensitized solar cells based on gel electrolytes containing different alkali metal iodide salts, Solid State Ionics 179 (2008) 2027–2030, https://doi.org/10.1016/J.SSI.2008.06.027.
[21] J.H. Kim, M.S. Kang, Y.J. Kim, J. Won, Y.S. Kang, Poly(butyl acrylate)/NaI/I2 electrolytes for dye-sensitized nanocrystalline TiO2 solar cells, Solid State Ionics 176 (2005) 579–584, https://doi.org/10.1016/J.SSI.2004.10.002.
[22] A.M. Abdullah, S.B. Aziz, S.R. Saeed, Structural and electrical properties of polyvinyl alcohol (PVA):Methyl cellulose (MC) based solid polymer blend electrolytes inserted with sodium iodide (NaI) salt, Arab. J. Chem. 14 (2021) 103388, https://doi.org/10.1016/J.ARABJC.2021.103388.
[23] V. Cyriac, Y.N. Ismayil, K. Sudhakar, Z.E. Mishra, M.S. Rojudi, I.M. Noor Murari, Effect of dopant on ion-dynamics of sodium ion-based flexible polyblend electrolyte for electrochemical device application, Mater. Res. Bull. 169 (2024) 112498, https://doi.org/10.1016/J.MATERRESBULL.2023.112498.
[24] J.B. Wagner, C. Wagner, Electrical conductivity measurements on cuprous halides, J. Chem. Phys. 26 (1957) 1597–1601, https://doi.org/10.1063/1.1743590.
[25] M. Kaya, S. Khadem, Y.S. Cakmak, M. Mujtaba, S. Ilk, L. Akyuz, A.M. Salaberria, J. Labidi, A.H. Abdulqadir, E. Deligöz, Antioxidative and antimicrobial edible chitosan films blended with stem, leaf and seed extracts of Pistacia terebinthus for active food packaging, RSC Adv. 8 (2018) 3941–3950, https://doi.org/10.1039/C7RA12070B.
[26] S.A. Riyajan, Environmentally friendly novel maleated poly(vinyl alcohol) grafted 1, 4-Butanediol modified with biopolymer for encapsulation of capsaicin, J. Polym. Environ. 27 (2019) 2637–2649, https://doi.org/10.1007/S10924-019-01542-8/TABLES/1.
[27] N.A.M. Zain, M.S. Suhaimi, A. Idris, Development and modification of PVA–alginate as a suitable immobilization matrix, Process Biochem. 46 (2011) 2122–2129, https://doi.org/10.1016/J.PROCBIO.2011.08.010.
[28] N.M.J.J. Rasali, Y. Nagao, A.S. Samsudin, Enhancement on amorphous phase in solid biopolymer electrolyte based alginate doped NH4NO3, Ionics (Kiel) 25 (2019) 641–654, https://doi.org/10.1007/s11581-018-2667-3.
[29] S. Safi, M. Morshed, S.A. Hosseini Ravandi, M. Ghiaci, Study of electrospinning of sodium alginate, blended solutions of sodium alginate/poly(vinyl alcohol) and sodium alginate/poly(ethylene oxide), J. Appl. Polym. Sci. 104 (2007) 3245–3255, https://doi.org/10.1002/APP.25696.
[30] S. Zhang, H. Dandan, D. Zongxian, W. Xin, Z. Dan, H.U. Yan, X. Xincai, Fabrication and Characterization of One Interpenetrating Network Hydrogel Based on Sodium Alginate and Polyvinyl Alcohol, (n.d.). doi:https://doi.org/10.1007/s11595-019-2112-0.
[31] A. Ahmad, Mohd Y. Abd Rahman, M. Su'ait, H. Hamzah, Study of MG 49-PMMA based solid polymer electrolyte, Open Mater. Sci. J. 5 (2011) 170–177.
[32] T. Çaykara, S. Demirci, Preparation and characterization of blend films of poly (vinyl alcohol) and sodium alginate 43 (2007) 1113–1121, https://doi.org/10.1080/10601320600740389.

[33] C. Chavan, R.F. Bhajantri, V. Cyriac, Ismayil, S.S. Bulla, K. Sakthipandi, Investigations on anomalous behavior of ionic conductivity in NaPF6 salt loaded hydroxyethyl cellulose biodegradable polymer electrolyte for energy storage applications, Polym. Adv. Technol. (2023), https://doi.org/10.1002/PAT.6004.

[34] T. Steiner, The hydrogen bond in the solid state, Angew. Chem. Int. Ed. Eng. 41 (2002) 49–76, https://doi.org/10.1002/1521-3773(20020104)41:1<48::AID-ANIE48>3.0.CO;2-U.

[35] M.M. Coleman, P.C. Painter, Hydrogen bonded polymer blends, Prog. Polym. Sci. 20 (1995) 1–59, https://doi.org/10.1016/0079-6700(94)00038-4.

[36] N. Zebardastan, M.H. Khanmirzaei, S. Ramesh, K. Ramesh, Presence of NaI in PEO/PVdF-HFP blend based gel polymer electrolytes for fabrication of dye-sensitized solar cells, Mater. Sci. Semicond. Process. 66 (2017) 144–148, https://doi.org/10.1016/J.MSSP.2017.04.016.

[37] J.-M. Yang, N.-C. Wang, H.-C. Chiu, Preparation and characterization of poly(vinyl alcohol)/sodium alginate blended membrane for alkaline solid polymer electrolytes membrane, J. Membr. Sci. 457 (2014) 139–148, https://doi.org/10.1016/j.memsci.2014.01.034.

[38] R.M. Hodge, G.H. Edward, G.P. Simon, Water absorption and states of water in semicrystalline poly(vinyl alcohol) films, Polymer (Guildf) 37 (1996) 1371–1376, https://doi.org/10.1016/0032-3861(96)81134-7.

[39] V. Cyriac, Ismayil, I.S.B.M. Noor, Z.E. Rojudi, Y.N. Sudhakar, C. Chavan, R. F. Bhajantri, M.S. Murari, Modification in the microstructure of sodium carboxymethylcellulose/polyvinyl alcohol polyblend films through the incorporation of NaNO3 for energy storage applications, Int. J. Energy Res. 46 (2022) 22845–22866, https://doi.org/10.1002/er.8588.

[40] S.B. Aziz, I. Brevik, M.H. Hamsan, M.A. Brza, M.M. Nofal, A.M. Abdullah, S. Rostam, S. Al-Zangana, S.K. Muzakir, M.F.Z.Z. Kadir, Compatible solid polymer electrolyte based on methyl cellulose for energy storage application: structural, electrical, and electrochemical properties, Polymers 12 (2020) 2257, https://doi.org/10.3390/POLYM12102257.

[41] L.P. Teo, M.H. Buraidah, A.F.M. Nor, S.R. Majid, Conductivity and dielectric studies of Li 2SnO 3, Ionics (Kiel) 18 (2012) 655–665, https://doi.org/10.1007/s11581-012-0667-2.

[42] J. Malathi, M. Kumaravadivel, G.M. Brahmanandhan, M. Hema, R. Baskaran, S. Selvasekarapandian, Structural, thermal and electrical properties of PVA–LiCF3SO3 polymer electrolyte, J. Non-Cryst. Solids 356 (2010) 2277–2281, https://doi.org/10.1016/J.JNONCRYSOL.2010.08.011.

[43] A. Manuel Stephan, R. Thirunakaran, N.G. Renganathan, V. Sundaram, S. Pitchumani, N. Muniyandi, R. Gangadharan, P. Ramamoorthy, A study on polymer blend electrolyte based on PVC/PMMA with lithium salt, J. Power Sources 81–82 (1999) 752–758, https://doi.org/10.1016/S0378-7753(99)00148-2.

[44] A.K. Arof, S. Amirudin, S.Z. Yusof, I.M. Noor, A method based on impedance spectroscopy to determine transport properties of polymer electrolytes, Phys. Chem. Chem. Phys. 16 (2014) 1856–1867, https://pubs.rsc.org/en/content/articlehtml/2014/cp/c3cp53830c (accessed June 29, 2021).

[45] B.N. Parida, P.R. Das, R. Padhee, R.N.P. Choudhary, Structural, dielectric and electrical properties of Li2Pb 2La2W2Ti4Nb4O 30 ceramic, Bull. Mater. Sci. 36 (2013) 883–892, https://doi.org/10.1007/S12034-013-0543-3/FIGURES/13.

[46] L. Essaleh, S. Amhil, S.M. Wasim, G. Marín, E. Choukri, L. Hajji, Theoretical and experimental study of AC electrical conduction mechanism in the low temperature range of p-CuIn3Se5, Phys. E Low Dimens Syst. Nanostruct. 99 (2018) 37–42, https://doi.org/10.1016/J.PHYSE.2018.01.012.

[47] S.N. Tripathy, Z. Wojnarowska, J. Knapik, H. Shirota, R. Biswas, M. Paluch, Glass transition dynamics and conductivity scaling in ionic deep eutectic solvents: the case of (acetamide + lithium nitrate/sodium thiocyanate) melts, J. Chem. Phys. 142 (2015), https://doi.org/10.1063/1.4919946/193708.

[48] S.K. Chaurasia, A.L. Saroj, V.K. Shalu, A.K. Singh, A.K. Tripathi, Y.L. Gupta, R.K. Singh Verma, Studies on structural, thermal and AC conductivity scaling of PEO-LiPF6 polymer electrolyte with added ionic liquid [BMIMPF6], AIP Adv. 5 (2015), https://doi.org/10.1063/1.4927768/22277.

[49] C.R. Mariappan, G. Govindaraj, Ac conductivity, dielectric studies and conductivity scaling of NASICON materials, Mater. Sci. Eng. B Solid State Mater. Adv. Technol. 94 (2002) 82–88, https://doi.org/10.1016/S0921-5107(02)00083-1.

[50] P. Rawat, A.L. Saroj, Effect of ionic liquid on plasticized CS-PVP-NaI based bio-polymer blend electrolytes: structural, thermal, dielectric and ion transport properties study, Mater. Sci. Eng. B 288 (2023) 116215, https://doi.org/10.1016/J.MSEB.2022.116215.

[51] M. Ravi, Y. Pavani, K. Kiran Kumar, S. Bhavani, A.K. Sharma, V.V.R. Narasimha Rao, Studies on electrical and dielectric properties of PVP:KBrO4 complexed polymer electrolyte films, Mater. Chem. Phys. 130 (2011) 442–448, https://doi.org/10.1016/J.MATCHEMPHYS.2011.07.006.

[52] S. Saha, T.P. Sinha, Dielectric relaxation in SrFe 1/2Nb 1/2O 3, J. Appl. Phys. 99 (2006), https://doi.org/10.1063/1.2160712/923115.

[53] S.B. Aziz, Role of dielectric constant on ion transport: reformulated Arrhenius equation, Adv. Mater. Sci. Eng. 2016 (2016), https://doi.org/10.1155/2016/2527013.

[54] M. Ravi, Y. Pavani, K. Kiran Kumar, S. Bhavani, A.K. Sharma, V.V.R. Narasimha Rao, Studies on electrical and dielectric properties of PVP:KBrO4 complexed polymer electrolyte films, Mater. Chem. Phys. 130 (2011) 442–448, https://doi.org/10.1016/J.MATCHEMPHYS.2011.07.006.

[55] S. Bhavani, M. Ravi, Y. Pavani, V. Raja, R.S. Karthikeya, V.V.R.N. Rao, Studies on structural, electrical and dielectric properties of nickel ion conducting polyvinyl alcohol based polymer electrolyte films, J. Mater. Sci. Mater. Electron. 28 (2017) 13344–13349, https://doi.org/10.1007/S10854-017-7171-4/FIGURES/6.

[56] N.A. Abdul Aziz, E.Z.M. Tarmizi, C.S.C. Razak, I.M. Noor, Impact of charge carrier transport properties on conductivity-temperature dependence of gellan gum-LiCF3SO3 biopolymer electrolyte, High Perform. Polym. 34 (2022) 691–700, https://doi.org/10.1177/09540083221102743/ASSET/IMAGES/LARGE/10.1177_09540083221102743-FIG 2.JPEG.

[57] T. Pongjanyakul, A. Priprem, S. Puttipipatkhachorn, Investigation of novel alginate−magnesium aluminum silicate microcomposite films for modified-release tablets, J. Control. Release 107 (2005) 343–356, https://doi.org/10.1016/J.JCONREL.2005.07.003.

[58] J.P. Soares, J.E. Santos, G.O. Chierice, E.T.G. Cavalheiro, Thermal behavior of alginic acid and its sodium salt, Eclética Química 29 (2004) 57–64, https://doi.org/10.1590/S0100-46702004000200009.

[59] R. Baskaran, S. Selvasekarapandian, N. Kuwata, J. Kawamura, T. Hattori, ac impedance, DSC and FT-IR investigations on (x)PVAc–(1 − x)PVdF blends with LiClO4, Mater. Chem. Phys. 98 (2006) 55–61, https://doi.org/10.1016/J.MATCHEMPHYS.2005.08.063.

[60] V. Cyriac, Ismayil, I.M. Noor, K. Mishra, C. Chavan, R.F. Bhajantri, S.P. Masti, Ionic conductivity enhancement of PVA: carboxymethyl cellulose poly-blend electrolyte films through the doping of NaI salt, Cellulose 29 (2022) 3271–3291, https://doi.org/10.1007/s10570-022-04483-z.

[61] M.F. Shukur, R. Ithnin, H.A. Illias, M.F.Z. Kadir, Proton conducting polymer electrolyte based on plasticized chitosan–PEO blend and application in electrochemical devices, Opt. Mater. (Amst) 35 (2013) 1834–1841, https://doi.org/10.1016/J.OPTMAT.2013.03.004.

[62] M.H. Khanmirzaei, S. Ramesh, Studies on biodegradable polymer electrolyte rice starch (RS) complexed with lithium iodide, Ionics 20 (2013) 691–695, https://doi.org/10.1007/S11581-013-1031-X.

[63] S.K.S. Basha, M.C. Rao, Spectroscopic and electrochemical properties of PVP based polymer electrolyte films, Polym. Bull. 8 75 (2017) 3641–3666, https://doi.org/10.1007/S00289-017-2229-2.

[64] S.K.S. Basha, G.S. Sundari, K.V. Kumar, M.C. Rao, Preparation and dielectric properties of PVP-based polymer electrolyte films for solid-state battery application, Polym. Bull. 75 (2017) 925–945, https://doi.org/10.1007/S00289-017-2072-5.

[65] A.J. Nagajothi, R. Kannan, S. Rajashabala, Preparation and characterization of PEO-based composite gel-polymer electrolytes complexed with lithium trifluoro methane sulfonate, Mater. Sci. Pol. 36 (2018) 185–192, https://doi.org/10.1515/MSP-2018-0025.

[66] P. Laha, A.B. Panda, S.K. Mahapatra, P.K. Barhai, A.K. Das, I. Banerjee, Development of rf plasma sputtered Al2O3–TiO2 multilayer broad band antireflecting coatings and its correlation with plasma parameters, Appl. Surf. Sci. 258 (2012) 2275–2282, https://doi.org/10.1016/J.APSUSC.2011.09.118.

[67] P.K. Singh, B. Bhattacharya, R.M. Mehra, H.W. Rhee, Plasticizer doped ionic liquid incorporated solid polymer electrolytes for photovoltaic application, Curr. Appl. Phys. 11 (2011) 616–619, https://doi.org/10.1016/J.CAP.2010.10.012.

[68] D.T. Hallinan, A. Rausch, B. McGill, An electrochemical approach to measuring oxidative stability of solid polymer electrolytes for lithium batteries, Chem. Eng. Sci. 154 (2016) 34–41, https://doi.org/10.1016/J.CES.2016.06.054.

[69] D. Bharati, A. Saroj, Plasticization effect of ionic liquid on structural, thermal and ion transport properties of CS-PVA-NaI based bio-polymer electrolyte membranes, 2023, pp. 1–19, https://doi.org/10.1080/25740881.2023.2175223.

[70] P.G. Bruce, J. Evans, C.A. Vincent, Conductivity and transference number measurements on polymer electrolytes, Solid State Ionics 28–30 (1988) 918–922, https://doi.org/10.1016/0167-2738(88)90304-9.

[71] P.B. Bhargav, V.M. Mohan, A.K. Sharma, V.V.R.N. Rao, Investigations on electrical properties of (PVA:NaF) polymer electrolytes for electrochemical cell applications, Curr. Appl. Phys. 9 (2009) 165–171, https://doi.org/10.1016/J.CAP.2008.01.006.

[72] V. Cyriac, S. Molakalu Padre, Ismayil, G. Sangam Chandrashekar, C. Chavan, R. Fakeerappa Bhajantri, M.S. Murari, Tuning the ionic conductivity of flexible polyvinyl alcohol/sodium bromide polymer electrolyte films by incorporating silver nanoparticles for energy storage device applications, J. Appl. Polym. Sci. 139 (2022) e52525, https://doi.org/10.1002/APP.52525.

[73] F. Gebert, J. Knott, R. Gorkin, S.-L.L. Chou, S.-X.X. Dou, Polymer electrolytes for sodium-ion batteries, Energy Storage Mater. 36 (n.d.) 10–30.

[74] L. Fan, S. Wei, S. Li, Q. Li, Y. Lu, Recent progress of the solid-state electrolytes for high-energy metal-based batteries, Adv. Energy Mater. 8 (2018) 1702657, https://doi.org/10.1002/aenm.201702657.

[75] M. Raja, A.M. Stephan, Natural, biodegradable and flexible egg shell membranes as separators for lithium-ion batteries, RSC Adv. 4 (2014) 58546–58552, https://doi.org/10.1039/c4ra08491h.

[76] Y. Zhu, F. Wang, L. Liu, S. Xiao, Z. Chang, Y. Wu, Composite of a nonwoven fabric with poly(vinylidene fluoride) as a gel membrane of high safety for lithium ion battery, Energy Environ. Sci. 6 (2013) 618–624, https://doi.org/10.1039/C2EE23564A.

[77] Y. Zhu, Y. Yang, L. Fu, Y. Wu, A porous gel-type composite membrane reinforced by nonwoven: promising polymer electrolyte with high performance for sodium ion batteries, Electrochim. Acta 224 (2017) 405–411, https://doi.org/10.1016/J.ELECTACTA.2016.12.030.

[78] J. Zhang, H. Wen, L. Yue, J. Chai, J. Ma, P. Hu, G. Ding, Q. Wang, Z. Liu, G. Cui, L. Chen, In situ formation of polysulfonamide supported poly(ethylene glycol) divinyl ether based polymer electrolyte toward monolithic sodium ion batteries, Small 13 (2017) 1601530, https://doi.org/10.1002/SMLL.201601530.

[79] T. Gasti, V.D. Hiremani, S.S. Kesti, V.N. Vanjeri, N. Goudar, S.P. Masti, S. C. Thimmappa, R.B. Chougale, Physicochemical and antibacterial evaluation of poly (vinyl alcohol)/guar gum/silver nanocomposite films for food packaging applications, J. Polym. Environ. 29 (2021) 3347–3363, https://doi.org/10.1007/S10924-021-02123-4/TABLES/4.